Fall 2011

Impact effects of explosively formed projectiles on normal and high strength concrete

Laurin Ashley Bookout

Recommended Citation

Bookout, Laurin Ashley, "Impact effects of explosively formed projectiles on normal and high strength concrete" (2011). *Masters Theses*. 6910.
https://scholarsmine.mst.edu/masters_theses/6910

IMPACT EFFECTS OF EXPLOSIVELY FORMED PROJECTILES ON NORMAL AND HIGH STRENGTH CONCRETE

by

LAURIN ASHLEY BOOKOUT

A THESIS

Presented to the Faculty of the Graduate School of the

MISSOURI UNIVERSITY OF SCIENCE AND TECHNOLOGY

In Partial Fulfillment of the Requirements for the Degree

MASTER OF SCIENCE IN EXPLOSIVES ENGINEERING

2011

Approved by

Dr. Jason Baird, Advisor
Dr. Paul Worsey
Dr. Jeffery Volz

ABSTRACT

The ability to quickly estimate the damage that a projectile will do to a structure is highly desired for structures that will be required to resist threats of this nature. There are several formulas for concrete penetration due to projectile impact that are based on empirical data. However, there is a lack of publicly available data for projectile impacts with striking velocities that exceed 1 km/s and have weights greater than a few grams. This research is intended to expand the available data on explosively formed projectile impacts and determine which, if any, of the existing equations can be used or slightly modified to predict penetration depths. In order to determine un-deformed measurements for the explosively formed projectiles, five projectiles were recovered using a soft recovery system. Then, multiple shots were performed using blocks of normal and high strength concrete. The projectiles remained consistent throughout all of the shots.

ACKNOWLEDGMENTS

First, I would like to express my sincere appreciation to my advisor, Dr. Jason Baird for his support, guidance, and patience over these past two years. Without him, this research could not have been completed. I would also like to thank Dr. Paul Worsey and Dr. Jeffery Volz for their advice support throughout the project.

I am very thankful the assistance I received from DeWayne Phelps, Jimmie Taylor Sr., Phillip Mulligan, Chris Searing, Alex Tyson, Matt Coy, Mike Allen, Matt Ortel, John Bullock and the Engineering Research Lab staff during testing and other phases of this research.

I also appreciate all the hard work and effort by Dr. Samuel Frimpong, Dr. Paul Worsey, Dr. Gillian Worsey, and everyone else that helped to establish the M.S. in Explosives Engineering as well as the efforts of Barbara Robertson, Shirley Hall, and Judy Russell who do excellent job keeping the department running smoothly.

Finally, I would like to thank my family and friends for their support and encouragement during my time at UMR/Missouri S&T.

TABLE OF CONTENTS

Page

SECTION

LIST OF ILLUSTRATIONS

LIST OF TABLES

NOMENCLATURE

Symbol	Description
AFRL	Air Force Research Lab
C-4	Composition 4
CD	Charge diameter
CRH	Caliber Radius Head
CSC	Conical shaped charge
cm	Centimeter
D	Caliber density
EFP	Explosively formed projectile
HRWR	High Range Water Reducer
HSC	High strength concrete
in.	Inch
ITZ	Interfacial transition zone
f'_c	Unconfined Compressive Strength for concrete, MPa or lb/in^2
ft	Foot or feet
ft/s	(Foot, feet)/second
K	Penetrability constant (UFC Formulas)
kg	Kilogram
km	Kilometer
km/s	Kilometer/second
lb	Pound
m	Meter
M_p	Projectile mass
NSC	Normal strength concrete
oz	ounce (weight)
psi	Pounds per square inch
s	Second
S.O.	Standoff distance
UFC	Unified Facilities Criteria

U_R	Rarefaction shock velocity
u_R	Rarefaction particle velocity
V_s	Projectile striking velocity
Wt	Weight
X_f	Penetration of fragment in inches (UFC formulas)
ρ_1	Shocked density
µs	Microsecond

1. INTRODUCTION

The ability to quickly and accurately estimate the concrete penetration depth of a certain projectile is desired for both offensive and defensive reasons. Unlike precision conical shaped charges (CSC) that require standoff distances (S.O.) that are between 5-8 charge diameters (CD) for optimal penetration, or non-precision CSC that obtain optimal penetration with a S.O. of roughly 2 CD, an explosively formed projectile (EFP) is a device that can effectively penetrate targets with standoff distances up to several hundred charge diameters. (1) EFPs also generate higher mass and larger diameter projectiles than CSCs do. The projectile generated by the detonation of an EFP is capable of delivering a large amount of energy to a concentrated area, which can compromise the integrity of all or part of a concrete structure, as shown in Figure 1.1. A CSC has a conical shaped liner, usually made of copper with explosive packed behind the liner, and produces a high speed jet of metal when the explosive detonates, while an EFP has a smoothly curved liner and produces a projectile upon detonation of the explosive. The term ‘flyer’ refers to the copper liner used in the EFP construction, before the explosive has been detonated, while ‘projectile’ refers to the copper liner after the explosive has been detonated. ‘EFP’ refers to the flyer and explosive charge situated within the casing.

Figure 1.1: Reinforced concrete after EFP impact.(2)

As the striking velocity V_s of a projectile increases, the overall structural response becomes secondary to the material properties at, and adjacent to, the impact point. For example, below 0.25 km/s (820 ft/s), structural dynamics can be used to predict the structural response. As the striking velocity increases from 0.5 km/s (1640 ft/s) to 2 km/s 6562 ft/s), the material behavior within and adjacent to the impact becomes more important than the response of the structure. (3) The velocities for the projectiles used in this research fall in the 0.5 km/s (1640 ft/s) to 2 km/s (6562 ft/s) range.

Since the material behavior becomes the most important factor for the estimation of projectile penetration, having a material with well-defined, consistent failure characteristics makes the prediction of the penetration depths simpler. Unlike most metals, concrete is both brittle and heterogeneous. The failure modes and strengths of brittle materials tend to be heavily influenced by small imperfections and flaws within the material, and this property of brittle materials can make the failure strengths and locations inconsistent. The brittle failure characteristics of concrete make predicting projectile penetration depths more difficult.

This research will compare existing equations for projectile penetration of concrete targets with experimental data in order to determine which, if any, of the equations can be used to estimate the penetration depths of EFPs. There has been much research done on projectile penetration of concrete as well as the response of concrete to hard projectile impact and attempting to predict the dynamic failure patterns of concrete. However, many of the current penetration equations for concrete state limitations for projectile striking velocity and projectile mass (M_p) that exclude the EFPs studied here. The experimental data gathered during this project will also expand the publicly available impact data for projectiles with striking velocities greater than 1 km/s. A larger selection of readily available experimental data dealing with impacts of this type will allow engineers to design a building subjected to EFP or similar threats to the necessary specifications to protect personnel and equipment.

2. LITERATURE REVIEW

2.1. EQUATIONS FOR PROJECTILE PENETRATION OF CONCRETE

2.1.1. Modified Petry Formula. Developed in 1910, the Petry Formula has been commonly used to determine local “hard” missile impacts. “Hard” missiles are classified as having small deformability relative to the target deformability. The penetration depth in inches is given by Equation 1, where K_p is the concrete penetration coefficient, A_p is the weight of the missile per unit area (lb/ft^2), and V_0 is the striking velocity in ft/sec.

$$\boldsymbol{x = 12K_pA_p\log_{10}(1+\frac{V_0^2}{215{,}000})} \qquad (1)$$

Originally the definition of K_p only related to the type of reinforcement, without considering the unconfined compressive strength (f'_c). The original K_p values are 0.00799 for massive concrete, 0.00426 for normal reinforced concrete, and 0.00284 for specially reinforced concrete. (4) Amirikan later revised K_p to account for the concrete strength in specially reinforced concrete, although the revised K_p values are sometimes used for normal reinforced concrete. The graph of the K_p values revised by Amirikan can be found in Reference (4).

2.1.2. Modified NDRC Formula. In 1946, the National Defense Research Committee proposed a formula for a non-deforming projectile penetrating a massive concrete target. Readily available experimental data from various tests provided the results used to develop this empirical formula. The NDRC equation is presented in Equation 2, with the missile shape factor, N*, defined in Equation 3, and the G-function, $G_{(x/d)}$, defined in Equation 4, where d is the diameter of the projectile in inches, W is the weight of the projectile in pounds, V_0 is the striking velocity of the projectile, in ft/sec, and x is the penetration depth of the projectile in inches. (5)

$$\boldsymbol{G_{(x/d)} = KN^{*}d^{0.2}\left(\frac{W}{d^3}\right)\left(\frac{V_0}{1000}\right)^{1.80}} \qquad (2)$$

$$\boldsymbol{N^* = 0.72 + 0.25\sqrt{n - 0.25}} \tag{3}$$

$$\boldsymbol{G_{(x/d)} = \begin{cases} (x/2d)^2, & x/d < 2.0 \\ [(x/d) - 1], & x/d \geq 2.0 \end{cases}} \tag{4}$$

The concrete penetrability factor, K, remained unavailable to the public until Kennedy defined K in relation to the concrete compressive strength, f'_c in psi, as shown in Equation 5. (4)

$$\boldsymbol{K = \frac{180}{\sqrt{f'_c}}} \tag{5}$$

Combining the original NDRC formula in Equation 2 with Equation 5, results in what is referred to the as the Modified NDRC Formula.

2.1.3. Whiffen Formula. Using penetration data of fragments and bombs striking reinforced concrete, the Whiffen Formula expanded the applicability of the prediction equations to larger projectile diameters. The Whiffen Formula also includes a factor based on the concrete aggregate size. (6) The limitations of the formula, shown in Equation 6, are as follows:

$800 < f'_c$ (concrete compressive strength) $< 10{,}000$ psi
$0.3 < M$ (mass of the projectile) $< 22{,}000$ lb
$0.5 < d$ (diameter of the projectile) < 38 in.
$0 < V_0$ (striking velocity of the projectile) < 1750 ft/s
$0.5 < d/a$ (a is the maximum aggregate size (in,) < 3.5

$$\boldsymbol{\frac{x}{d} = \left(\frac{870}{\sqrt{f'_c}}\right)\left(\frac{M}{d^3}\right)\left(\frac{d}{a}\right)^{0.1}\left(\frac{V_0}{1750}\right)^{n} \quad where \quad n = \frac{10.70}{\sqrt{f'_c}}} \tag{6}$$

2.1.4. Kar Formula. The Kar Formula, while very similar to the 1946 NDRC Formula, accounts for the type of missile material in terms of Young's modulus. Predicting the penetration depth missile made of steel with both the NDRC and Kar formulas would yield the same result. (6) The Kar Formula is represented by Equation 7, where E_s represents the Young's modulus of steel in either psi or ksi, and E represents the Young's modulus of the missile material in the same units as E_s. The nose shape factor, N^*, was previously defined in Equation 3, M is the projectile weight in pounds, d the projectile diameter in inches, f'_c is the concrete compressive strength in psi, and V_0 represents the striking velocity of the projectile in ft/s.

The G-factor calculated from Equation 7 would then be used in Equation 4 to obtain the predicted penetration depth.

$$\boldsymbol{G_{(x/d)} = \frac{180N^*M}{d\sqrt{f'_c}}\left(\frac{E}{E_s}\right)^{1.25}\left(\frac{V_0}{1000d}\right)^{1.8}} \tag{7}$$

2.1.5. Amman and Whitney Formula. The Amman and Whitney Formula can be used to predict the penetration of small, explosively formed fragments travelling over 305 m/s (1000 ft/s). (6) This formula is shown in Equation 8 where x is the penetration depth in inches, and all other variables are as defined previously in Section 2.1.4.

$$\boldsymbol{\left(\frac{x}{d}\right) = \frac{282}{\sqrt{f'_c}}N^*\left(\frac{M}{d^3}\right)d^{0.2}\left(\frac{V_0}{1000}\right)^{1.8}} \tag{8}$$

2.1.6. Forrestal, 1994. Forrestal, et al. derived an equation to predict the penetration of ogival rods into concrete targets. The equation uses readily available unconfined compressive concrete strengths along with a dimensionless constant S, instead of tri-axial test data that is commonly used for computational model inputs. (7) The graph in Figure 2.1, taken directly from Reference (7) allows for the estimation of S based on the f'_c of the concrete.

After determining S using Figure 2.1 and the measured f'_c, the penetration of the projectile, in meters, can be estimated using Equations 9, 10, and 11. For Equations 9, 10, and 11, ψ represents the caliber-radius head of the projectile (0.5 for hemispherical projectiles), m is the mass of the projectile in kilograms, a is the diameter of the projectile in meters, f'_c is the concrete compressive strength in MPa, ρ is the concrete density in kg/m^3, V_s is the projectile striking velocity in m/s and P is the penetration depth in meters.

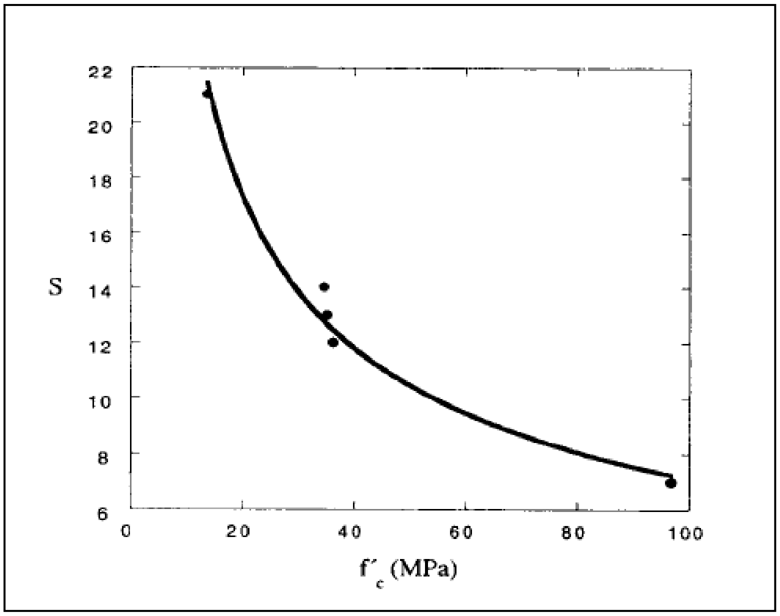

Figure 2.1: Dimensionless constant S based on f'$_c$.

$$N = \frac{8\psi - 1}{24\psi^2} \tag{9}$$

$$V_1^2 = \frac{m{V_s}^2 - 4\psi a^3 S f'_c}{m + 4\pi a^3 N\rho} \tag{10}$$

$$P = \frac{m}{2\pi a^2 \rho N} \ln\left(1 + \frac{N\rho V_1^2}{S f'_c}\right) + 4a \qquad P > 4a \tag{11}$$

2.1.7. Sandia Penetration Equations. In 1997, Sandia National Laboratories, NM, published penetration equations for various materials, including concrete. Equation 12 gives the penetration equation for a projectile moving faster than 200 (ft/s) and striking a soil, rock, or concrete target, where *D* is the penetration distance in feet, *W* is the weight of the projectile in pounds, *A* is the cross-sectional area of the penetrator, *V* is the striking velocity in ft/s, and K_h is a scaling term for projectile weights under 400 pounds.

$$\boldsymbol{D = \left[0.00178SN\left(\frac{W}{A}\right)^{0.7}(V-100)\right]K_h} \tag{12}$$

The terms *S* (for concrete), *N*, and K_h used in Equation 12 are defined in Equations 13, 14, and 15 below. In Equation 13, *P* is the volumetric percent rebar, t_c is the cure time in years and must be ≤ 1, T_c is the thickness of the target in penetrator diameters, with a maximum value of 6, and K_e for unreinforced concrete equals $(30/W)^{0.3}$.

$$\boldsymbol{S = 0.085K_e(11-P)(t_cT_c)^{-0.06}\left(\frac{5000}{f'_c}\right)^{0.3}} \tag{13}$$

$$\boldsymbol{N = 0.18(CRH-0.25)^{0.5}+0.56} \tag{14}$$

$$\boldsymbol{K_h = 0.4W^{0.15} \quad when\ W \le 400\ lbs.} \tag{15}$$

If the equations are used within their stated limitations the accuracy of the result is within approximately 15%, except near the limits of applicability. The following limitations govern the applicable use of the Sandia penetration equations: (8)

-The penetrator remains intact during penetration

-The penetrator follows a basically stable trajectory

-The impact velocity is less than 4000 ft/s

-When the penetration depth is less than three calibers, the equations may be questionable

-The equations are not valid for materials other than those specifically listed

-Minimum penetrator weight for concrete is about 10 pounds

2.1.8. Unified Facilities Criteria Formula. The Unified Facilities Criteria (UFC) document UFC 3-340-02 compiles information on and provides guidelines for the design of structures to resist accidental explosions. This document contains a section to estimate fragment penetration of concrete based on projectile diameter, weight, striking velocity, nose shape, caliber density, and the unconfined compressive strength of the concrete. (9) For penetration of concrete by armor piercing fragments, the estimated depth can be estimated using Equation 16 or 17 in combination with Equation 18.

$$\boldsymbol{X_f = (4.0E^{-3})(KN^{*}D)^{0.5}d^{1.1}V_s^{0.9} \quad for\ X_f \leq 2d} \tag{16}$$

$$\boldsymbol{X_f = (4.0E^{-6})KN^{*}Dd^{1.2}V_s^{1.8} + d \quad for\ X_f > 2d} \tag{17}$$

$$\boldsymbol{K = \frac{12.91}{\sqrt{f'_c}}} \tag{18}$$

Where:

X_f = penetration by armor piercing steel fragments (in.)

K = penetrability constant

N^*= nose shape factor as defined in Equation 3

D= Caliber density, or W/d^3 (lb/in.^{3})

d= Fragment diameter (in.)

V_s= Striking Velocity (ft/s)

f'_c= concrete compressive strength (lb/in.^{2})

For the penetration of concrete by fragments other than armor piercing, the penetration can be adjusted to accommodate the fragment material with a constant. Equation 19 gives the estimated penetration of a non-armor piercing fragment.

$$\boldsymbol{X'_f = kX_f} \tag{19}$$

Where:

X'_f = maximum penetration of a non-armor piercing fragment

k = constant dependent upon the casing metal
X_f = penetration calculated by Equation 16 or 17

The given values of k, from Table 4-16 of Reference (9) are shown below.

Armor piercing steel, k = 1.0
Mild steel, k = 0.7
Lead, k = 0.5
Aluminum, k = 0.15

2.2. SOFT RECOVERY OF EFPs

2.2.1. Air Force Research Lab Method. In 2005, the Air Force Research Lab (AFRL) at Eglin Air force Base developed a method to safely recover EFPs while keeping them intact. To estimate penetration depths of the projectiles through different density materials, the researchers used a drag force model that they had previously developed and presented. .

An increasing density gradient along the projectile trajectory allowed the projectiles to be caught with minimal deformation. The materials used in the AFRL method include polystyrene (32 kg/m^3), vermiculite (126 kg/m^3), fiberboard (256 kg/m^3), water (1000 kg/m^3), and sand (1760-2080 kg/m^3). Ideally, the projectile would stop within the water section, providing a quenching step that prevents additional annealing, recrystallization, and/or grain growth. The sand section served as extra material to catch projectiles that penetrated past the water section.

Eight pairs of velocity screens, placed at 1.2 m (4 ft) intervals, allowed the researchers to compare the experimental arrival times and velocity of the projectile to the estimated times as it traveled through the materials. The water quenched projectiles allowed the material to be preserved and analyzed in an “as-formed” state. (10)

2.2.2. TNO Defence Security and Safety Method. Two researchers from the Netherlands used a simple system to capture EFPs after the flash x-ray portion of their experiment. The target tubes consisted of a PVC pipe filled with sawdust followed by a long steel tube filled with water. (11) The paper states that the system allowed the EFPs to be captured without deformation, however, no photographs of the recovered projectiles are included in the article.

3. EXPERIMENTAL PROCEDURE

3.1. EFP CONSTRUCTION

The construction of the EFP, which includes the manufacture of the flyer plate, casing material and configuration, explosive charge weight, and cap depth were adapted from research reported in Reference (12).

3.1.1. Flyer Plate. The flyer plates consisted of 6.35 mm (1/4 in.) thick oxygen-free high conductivity copper plate, with 99.99% purity, formed to the proper curvature. The process to create each individual flyer plate is as follows:

1. Cut 10.16 cm (4 in.) squares from the copper plate
2. Align the plate on the die and use a hydraulic press to form the plate curvature
3. Cut out the circular flyer from the square, formed plate
4. Sand the edges of the plate to achieve a smooth, circular flyer

The finished flyer plate has a diameter of 9.53 cm (3.75 in.) and a height of 22.2 mm (0.875 in.). Figure 3.1 shows a completed flyer, however it should be noted that the two scalloped edges of the pictured flyer are not part of the intended design, but are from the process of pressing a flat 10.16 cm (4 in.) copper square to the desired curved shape.

Figure 3.1: Completed flyer plate.

3.1.2. Casing and Explosive Fill. The EFP casing and explosive fill designs used in this research are also borrowed from previous work. (12) The PVC used for the EFP casing, while providing less confinement than a metal casing, also has a lower potential for generating safety hazards due to fragmenting of the case when the explosive charge is detonated. The EFP casing consisted of an 8.89 cm (3.5 in.) long, 10.16 cm (4 in.) diameter PVC pipe and two PVC end caps. One cap had a centered opening slightly smaller than the diameter of the flyer, which held the flyer in place, but did not impede the formation of the projectile. The other cap had a centered 7.9 mm (5/16 in.) hole to allow the detonator to be placed at the appropriate depth in the explosive.

The explosive charge for each EFP consisted of 0.867 kg (1 lb, 14.6 oz) of C-4. The placement of the C-4 in the PVC casing had to be performed carefully in order to achieve consistency between each EFP. The first layer of C-4 placed required the most care, as it had to fill the 3.18 mm (0.125 in.) gap between the flyer and casing without shifting the flyer off-center. The first C-4 portions consisted of small, rope like pieces placed and pressed between the outside edge of the flyer and the PVC casing. After placing the C-4 around the flyer, the process of placing the C-4 in the casing utilized roughly 1.27 cm (0.5 in.) layers of C-4, hand-packed, then further compacted using a flat bottomed packing tool. Visually checking the flyer location after compacting each layer helped to ensure the flyer stayed centered throughout the process.

3.1.3. Detonator Placement. The type of detonator used to initiate the explosive charge remained consistent for all shots. The desire to use readily available detonators resulted in the decision to use Dyno #1 MS Series Electric Detonators for all 25 shots. For each shot, the detonator was inserted to a depth of 1.27 cm (0.5 in.) into the explosive. To ensure the correct insertion depth for the cap, both the thickness of the top PVC end cap as well as the distance between the top of the PVC pipe casing and the top of the explosive must be considered. After collecting both of the above values using a set of calipers, the appropriate value can be transferred to the detonator using a pair of calipers and electrical tape. The length of the detonator inserted into the EFP is equal to the desired detonator depth plus the thickness of the PVC end cap plus the distance between the top of the explosive and the top of the PVC pipe casing. Figure 3.2 illustrates the distances described above.

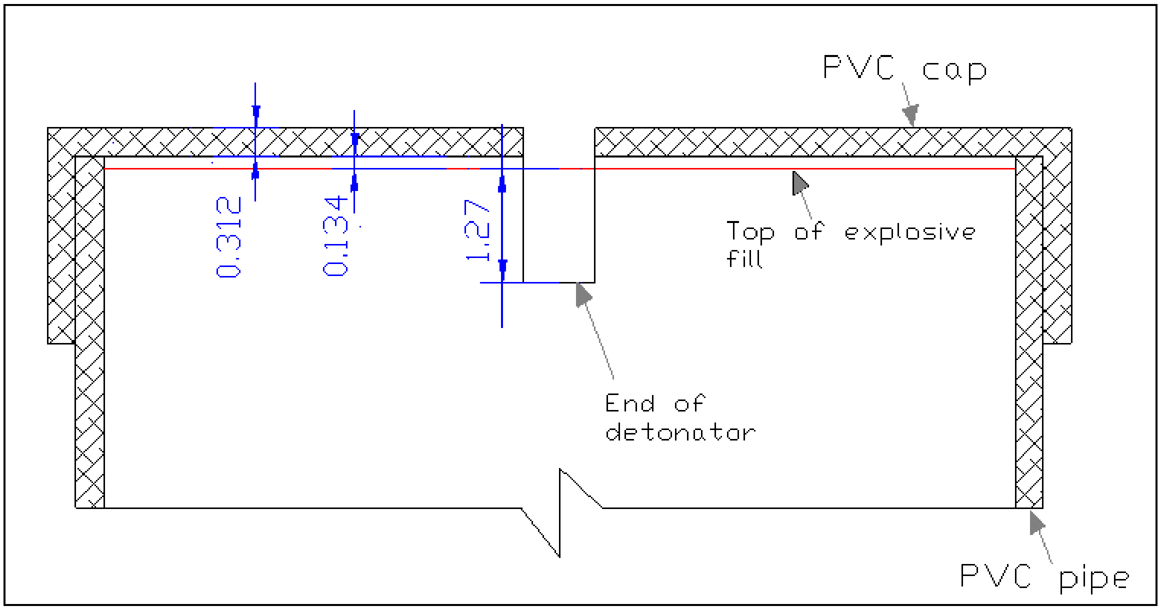

Figure 3.2: Distances required to find detonator depth below PVC cap (cm).

The detonator for an EFP with the physical parameters in Figure 3.2 would have a total detonator length of 1.72 cm (0.676 in.) inserted below the surface of the top PVC cap. The total length of 0.676 in. equals 0.123 in. plus 0.053 in. plus 0.5 in. Figure 3.3 shows the detonator before insertion; next, the detonator would be inserted until the edge of the electrical tape furthest from the leads aligned with the top of the PVC end cap.

3.2. SOFT RECOVERY

3.2.1. Material Selection and Placement. The soft recovery system used to capture the projectiles closely followed the setup developed by the Air Force Research Lab (AFRL) in 2005. The original research utilized an increasing density gradient along the projectile trajectory, allowing the projectiles to be caught with minimal deformation. The materials used in the AFRL were polystyrene (32 kg/m^3), vermiculite (126 kg/m^3), fiberboard (256 kg/m^3), water (1000 kg/m^3), and sand (1760-2080 kg/m^3). (10)

At the time of the testing, fiberboard with the correct density could not be obtained through local or other sources. So, other materials were considered for replacement based on their density, cost, and availability. Several materials that have a density comparable to the fiberboard are bamboo, cardboard, cork, and packed snow. Cardboard bales borrowed from a local recycling business replaced the fiberboard in the soft recovery setup for this research effort after considering both the density and the cost of the available materials.

Figure 3.3: Detonator ready for insertion.

The experimental data from the AFRL showed that the copper projectile stopped in the fiberboard section and did not achieve sufficient penetration to reach either the water or sand sections of the soft recovery system. Based on this data, the sand section was eliminated from the setup. Figure 3.4 shows the material layout of the soft recovery system, while Figure 3.5 shows a photo of the system before the first shot.

3.2.2. Experimental Setup and Execution. The soft recovery system was intended to successfully capture five projectiles without replacing any of the material. The final setup consisted of a 0.61 m (2 ft) square cross-section of polystyrene and vermiculite followed by two 1.8 m x 1.2 m x 1.2 m (6 ft x 4 ft x 4 ft) cardboard bales and a water barrel. Based on the experimental AFRL data, the projectiles were expected to be contained within the cardboard bales, but the water barrel served to catch any projectile that exceeded the expected penetration. The aligned and leveled polystyrene and vermiculite sections, along with the water barrel, provided a straight path for the projectile to travel through. The placement of the cardboard bales for the first shot aligned the edge of the bale with the edge of the soft recovery frame.

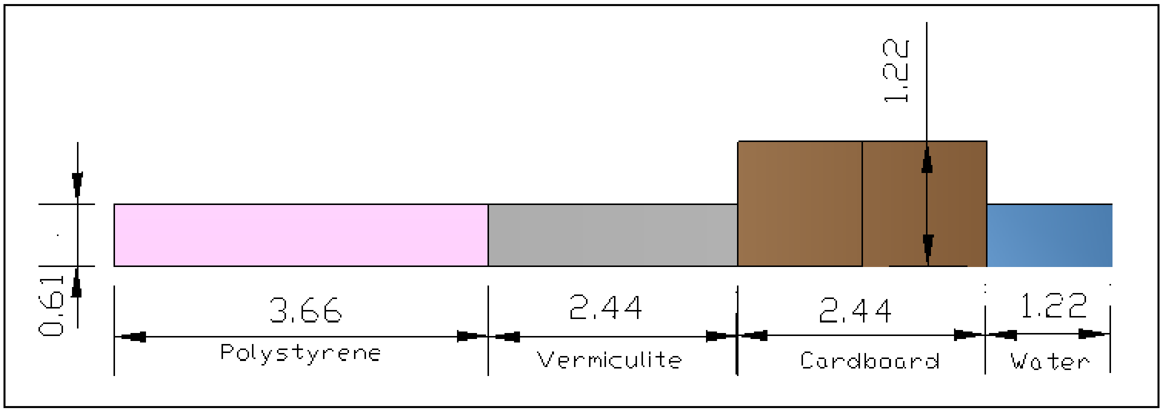

Figure 3.4: Soft recovery material layout (m).

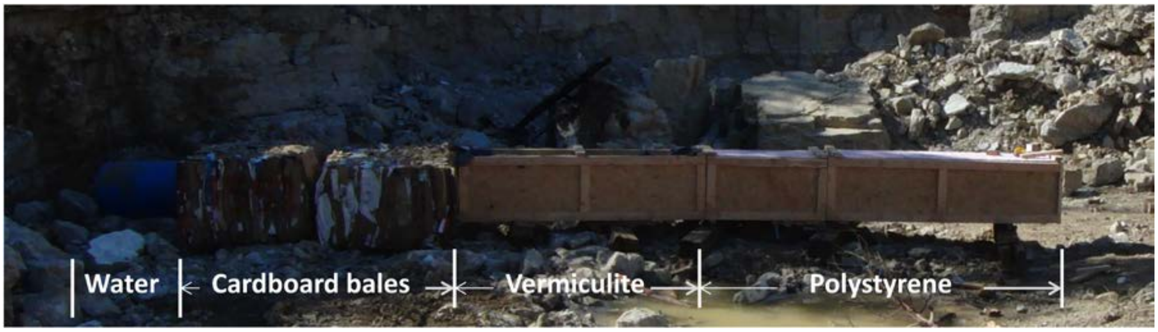

Figure 3.5: Soft recovery system.

The EFPs were mounted and aimed following the procedures outlined in detail in Section 3.4.2, and a digital high speed camera captured the projectile velocities. Using an assumed maximum velocity of 1317 m/s (4500 ft/s), based on previous research, the 5.64 m (18.5 ft) standoff distance allowed a sufficient amount of time for the flyer to invert and form the projectile before impacting the polystyrene.

After each shot the bales were moved perpendicularly to the projectile path so that the projectile would impact a new section of bale. Moving the bale after each shot prevented a projectile from striking a previously captured projectile upon entering the bale. After completing the five shots, the bale was disassembled in order to recover the projectiles.

The soft recovery system successfully captured all five of the projectiles within the first cardboard bale. The projectiles cooled while they rested in the cardboard bale; no quenching of the projectiles occurred. After disassembling the bale to recover the projectiles, a combination of hand-cleaning and an ultrasonic vinegar bath removed most of the foreign matter from each projectile.

3.3. CONCRETE BLOCK SPECIFICATIONS

3.3.1. Block Dimensions and Casting Process. Each of the concrete blocks had the dimensions 0.46 m x 0.46 m x 0.58 m (18 in. x 18 in. x 23 in.). Considerations that influenced the block size included availability of concrete forms, available equipment lifting capacity, and expected penetration depth of the projectiles. Each block had a small loop of rebar placed in the top middle that allowed the blocks to be easily lifted with a forklift and chain. The blocks contained no other reinforcing materials.

Two sets of forms 2.44 m long, 0.61 m wide, and 0.46 m deep (8 ft long, 2 ft wide, 1.5 ft deep) with plywood dividers every 0.46 m (1.5 ft) allowed for a minimal amount of formwork to be used during the concrete placement. Spacers used on the sides of the formwork to hold the dividers in place during concrete placement accounted for 2.54 cm (1 in.) of space, resulting in a final block length of 0.58 m (23 in.). Vibration of the concrete helped prevent voids and segregation of the aggregate along the bottom and sides of the blocks. Trowel finishing of the tops of the blocks resulted in a fairly smooth top surface.

The high strength concrete blocks remained covered with wet burlap for the first 24 hours after the pour due to cracking concerns from a high heat of hydration, while the normal strength blocks cured uncovered.

3.3.2. Normal Strength Concrete Mix Design. The target unconfined compressive strength of the normal strength concrete blocks was 3600 psi. Since the concrete would be unreinforced, the cementitious materials consisted of 20% flyash by weight. Flyash helps to lower the heat of hydration by slowing the hydration process. A lower heat of hydration reduces the chances of stress cracks forming on the surface and within the block as the concrete cures. Following the ACI 211.1 Mix Design guidelines yields the following mix design, shown in Table 3.1.

Table 3.1: Normal Strength Concrete Design

	kg/m^3	lb/yd^3
Coarse Aggregate	1211	2047
Water	181	306
Flyash (20%)	61	103
Portland Cement, Type 1	241	407
Fine Aggregate	656	1109
Water-Cement Ratio	0.6	0.6
Total Weight	**2350**	**3972**

3.3.3. High Strength Concrete Mix Design. The desired minimum unconfined compressive strength of the high strength concrete was 7000 psi. Both ACI 211.1 and data from previous pours were used in the high strength mix design. The material proportions are shown in Table 3.2.

3.4. FIELD TEST SETUP AND PROCEDURES

3.4.1. Target Placement. Each concrete block was placed on a gravel pad and leveled in both the front/back and left/right directions. One of the 0.46 m x 0.46 m

(18 in. x 18 in.) block faces served as the target face. The front face of the block did not have any gravel or other obstructions between it and the EFP. A 5.1 cm (2 in.) grid painted on both the front and back block faces along with numbers on each corner of the block allowed the main broken pieces to be identified after the shot. The grid also provided an easily identifiable scale reference in the experimental photos

Table 3.2: High Strength Concrete Mix Design

	kg/m^3	lb/yd^3
Coarse Aggregate	1131	1917
Water	150	255
Flyash (20%)	100	170
Portland Cement, Type 1	401	680
HRWR dose (quart/m^3 or yd^3)	0.33	0.44
Fine Aggregate	621	1048
Water-Cement Ratio	0.3	0.3
Total Weight	**2414**	**4070**

3.4.2. EFP Placement. Due to safety concerns and the desire to accurately aim the EFP, a cost-effective, disposable mount was used, rather than other reusable, but potentially risky systems. The mounting system for each EFP consisted of a wooden frame and a 22.9 cm x 45.7 cm (9 in. x 18 in.) sheet of polystyrene with a 10.16 cm (4 in.) hole cut in the center to allow the EFP to be mounted. The height of the EFP mount equaled the height of the block, allowing the EFP to be easily aimed at the center of the block while keeping the striking angle close to 0° measured from the horizontal. The detonation completely destroyed the EFP mount, but had less potential to produce dangerous fragments than a failed mount made of metal. An EFP placed in the mount is shown in Figure 3.6.

Figure 3.6: EFP positioned in mount.

3.5. INSTRUMENTATION

3.5.1. High Speed Camera. A Phantom model V5.1 high speed camera recorded each of the 25 shots to obtain the striking velocity of each projectile, a necessary value for the penetration calculations. The camera was placed approximately 30.5 m (100 ft) from the location of the EFP to help avoid damage to the camera system due to airblast or fragments. A metal box with a Plexiglas viewport shielded the camera from any small fragments. Ethernet cables connecting the camera to a laptop allowed the camera to be adjusted and triggered from a safe area during the tests. The settings for the camera for each shot are listed below.

-Lens type: Nikon
-Pictures per second (pps): 8000
-Exposure time: 20 μs
-Resolution: 512 x 256
-Total Frames: 16,216
-Post-Trigger Frames: 11,351 or 12,972

A reference board painted with a series of 8.26 cm (3.25 in.) and 1.91 cm (0.75 in.) stripes placed within view of the camera served to provide reference distances for velocity measurements. The placement of the reference board was such that it was perpendicular to the camera and parallel to the expected trajectory of the projectile.

3.5.2. Oscilloscope. For shots 16-25, a four-channel oscilloscope and two velocity screens provided an additional method of measuring projectile velocity. An oscilloscope connected to two disposable velocity screens placed at known distances from each other allowed a velocity to be calculated based on the times that the oscilloscope recorded a drop in voltage. The oscilloscope measurements should theoretically provide velocity measurements with a lower percent error that the high speed camera.

3.5.2.1 Velocity Screen Construction and Placement. The construction of each velocity screen consisted of a wooden frame with legs, and enamel-insulated 30 gage wire. The wooden frames had a 22.9 cm by 45.7 cm (9 in. by 18 in.) opening with wire strung vertically along the length of the frame. The first version of velocity screen, used in shots 16-20, had wire spacing of 12.7 mm (0.5 in.) along the length of the frame. The second version of velocity screen, used in shots 21-25, had wire spacing of 9.5 mm (0.375 in.) along the middle 10.16 cm (4 in.) of the frame, with 12.7 mm (0.5 in.) spacing on the outer edges. The wire strands did not overlap with one another to help prevent unintended completion of the circuit in the event that the insulation failed. A completed velocity screen is pictured in Figure 3.7.

For each shot, velocity screens were placed 1.83 m and 2.74 m (6 ft and 9 ft) away from the front edge of the EFP. The screens were placed exactly 0.91 m (3 ft) apart, and the measurements were double checked before leaving the blast area.

3.5.2.2 Oscilloscope and Velocity Screen System. Using one oscilloscope channel for each velocity screen allowed for the times of the voltage drops to be compared. An Ethernet cable strung from the blast site to the power source transmitted the voltage readings with very little noise. The final circuit consisted of the oscilloscope connected to the power source, the Ethernet cable running from the power source to the blast site, and then sacrificial wires connecting the Ethernet cable to the velocity screens. A diagram of the circuit is pictured in Figure 3.8.

Figure 3.7: Velocity screen.

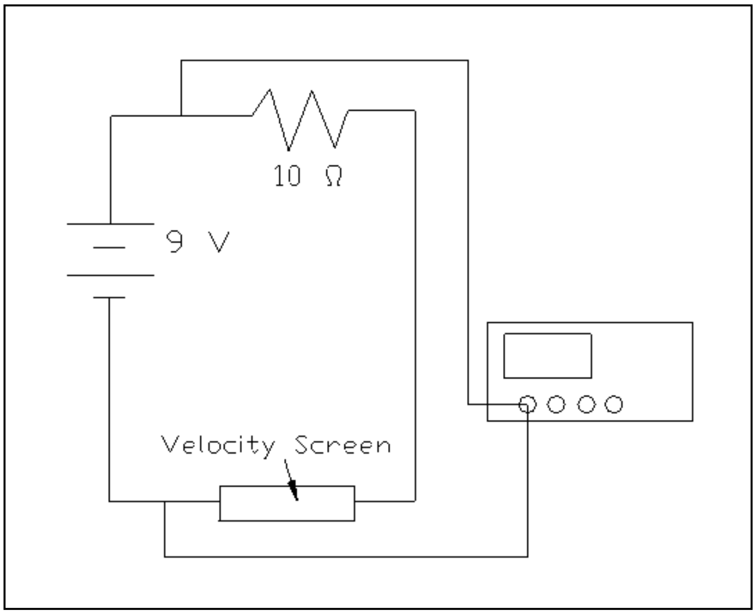

Figure 3.8: Oscilloscope/Velocity Screen Circuit.

Electrical tape secured the sacrificial wires to the Ethernet cables and the ends of the velocity screen wire. Placing the velocity screen wire connections on the back of the frame and securing them in several locations along the length of the frame helped prevent a false trigger due to an early cutoff or broken connection. Where necessary, a combination of timbers, dirt, and gravel protected the Ethernet cable, the sacrificial cables, and their connection from fragments and from being whipped around by the airblast.

3.6. CONCRETE VOLUME AND CRATER DEPTH MEASUREMENTS

3.6.1. Crater Depth Measurements. After the shot, the shattered front face of the block could not provide a surface from which to measure the crater depths. So, a wooden jig whose internal measurements matched the original block dimensions provided a consistent way to determine the crater depths. The wooden jig fit over the remaining block pieces. The top surface of the jig contained slots that allowed a yardstick to be inserted, flush with the surface of the jig, into the jig at 5.1 cm (2 in.) intervals. Measuring the crater depths on a 5.1 cm (2 in.) grid and at the impact point provided enough points to approximate the shape of the fractured surface, if necessary.

The following steps describe the process used to gather the crater depths:

- Piece together the remaining pieces of the back face of the block, fractured side facing up
- Place the jig over the block pieces, verifying centered and level placement of the jig
- Insert the yardstick into the first slot, noting the value of the yardstick at the interior, left-side of the jig
- Measure down from the top of the yardstick to the surface of the block
- Repeat measurements every two inches, from left to right, along the block
- Move the yardstick to the next slot
- Repeat the previous two steps until all the measurements along a 5.1 x 5.1 cm (2 x 2 in.) grid are complete
- Be sure to measure the depth at the impact point, regardless of whether it lands on the previously defined measurement grid

3.6.2. Concrete Volume Measurements. Employing the Archimedes Principle results in an easy way to measure the volume of an irregularly shaped object. The Archimedes Principle states that a submerged object will displace a volume of water equal to its own. Since the density of both the water and concrete are known, and the volume of water displaced by the concrete can be easily measured, calculating the remaining volume of concrete becomes simple.

Since the volume measurement of the remaining concrete is intended to determine how much concrete broke away from the block upon impact, only the pieces from the back face of the block are used. The following steps describe the process used to measure the volume of the remaining concrete block pieces.

- Fill a container with water, enough to cover the concrete, but not so much that the container will overflow.
- Mark the original water line with a grease pencil.
- Place the concrete pieces of one block in the container (performed multiple times per block due to the small container size) taking care not to deform the container shape with the concrete.
- Wait until the water surface becomes still again, and mark the final water line with a grease pencil- mark this line with the block number.
- Remove the concrete pieces from the container.
- Wait until the water surface becomes still again and refill the container, if necessary, so that the water level meets the original water line.
- Repeat the previous four steps until all of the concrete pieces have been submerged and all of the final water lines have been marked.
- Starting with the water level meeting the original water line, measure the weight of the water needed to fill the container to each individual final water line.
- Calculate the volume of concrete by Equation 20.

$$V_{concrete} = \frac{Wt_{water}}{\rho_{water}} \tag{20}$$

4. EXPERIMENTAL RESULTS

4.1. SOFT RECOVERY

The soft recovery system caught all five projectiles within the first cardboard bale. None of the projectiles exited the system prematurely, nor did any pass through the cardboard to the water barrel. However, Projectile 3 may have struck one of the framing members on the vermiculite section, as suggested by damage to the vermiculite section after the shot, as well as damage on one side of Projectile 3.

The penetration prediction equations require a “missile shape factor” for each projectile. The nose shape of the projectile is a variable used to calculate the missile shape factor. To determine the nose shape of each projectile, multiple projectile diameter measurements, taken along the length of the projectile were used to create a 2D projectile cross-section in SolidWorks ®. The SolidWorks ® product used was a drafting software with 2D and 3D capabilities.

The weights, along with the nose radius of each projectile, obtained after removing the foreign material, are compiled in Table 4.1. The cross-section of a recovered projectile, shown side by side with the recovered projectile in Figure 4.1, demonstrates the hemispherical shape of the projectile nose. The SolidWorks cross-section does not show the entire length of the projectile, since the tail shape does not need to be included to determine the nose radius

The five recovered projectiles are very similar to each other, although the lengths and widths vary somewhat. Projectiles 1-5 are numbered and shown in Figure 4.2 on a 2.54 cm (1 in.) grid. The damage that occurred on Projectile 3 from when it struck a framing member of the soft recovery system is visible.

While difficult to see in Figure 4.2, each recovered projectile has an air cavity which begins at the tail and progresses for an unknown distance forward into the projectile. In Figure 4.2, the photograph of Projectile 1 shows the clearest view of the start of the air cavity at the tail. The presence of the air cavity reveals that the flyer did not collapse completely during formation.

Table 4.1: Recovered projectile weights and nose radii

Flyer #	Initial Wt. (kg)	Initial Wt. (lb)	Final Wt. (kg)	Final Wt. (lb)	Wt. Loss (kg)	Wt. Loss (lb)	Nose Radius (m)	Nose Radius (in.)
1	0.453	1.000	0.381	0.840	0.072	0.160	0.012	0.46
2	0.448	0.990	0.374	0.825	0.075	0.165	0.013	0.51
3	0.451	0.995	0.371	0.820	0.079	0.175	0.013	0.50
4	0.451	0.995	0.371	0.820	0.079	0.175	0.013	0.50
5	0.451	0.995	0.371	0.820	0.079	0.175	0.010	0.41
				Averages	**0.077**	**0.170**	**0.012**	**0.48**

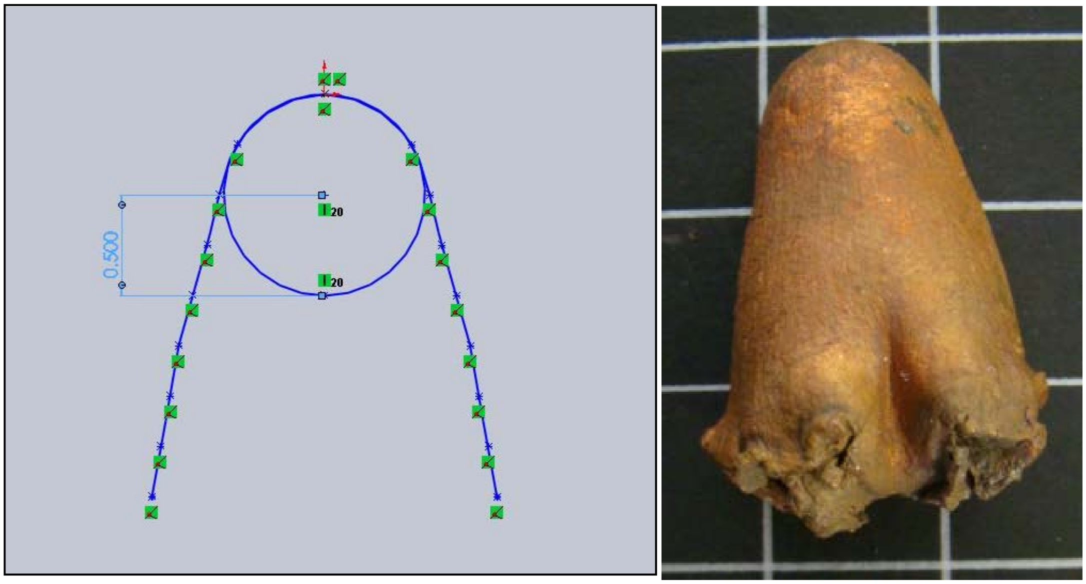

Figure 4.1: Projectile 3 and its cross section (inches).

4.2. NORMAL STRENGTH CONCRETE TESTS

For all ten normal strength concrete block tests, the projectile impacted the block. The impact of the projectile resulted in the complete fracture of the front one-half to two-thirds of the block. The concrete that formed the front part of the block scattered around the test site, while the back part of the block broke into multiple recognizable pieces. The pieces from the back of the block could be placed back together, which allowed the fracture pattern to be clearly viewed. On most of the blocks, the impact of the projectile occurred within 10.2 cm (4 in.) of the central point. On three of the targets, off-center impact location caused the back of the target not to fracture, or to break into only two pieces.

Figure 4.2: Recovered Projectiles 1-5.

The location of where the fractures join, and where some concrete may be missing corresponds to the impact point of the projectile on the front of the block. Assuming that the impact point and the location of the spall are directly opposite each other allows for the easy determination of the impact point, based on the photos of the blocks after the shots. The reasoning for assuming that the impact point and spall area are directly opposite each other is addressed in the Discussion section, Section 5. The grids painted on the blocks are 5 cm (2 in.).

4.2.1. Concrete Compressive Strength. The measurement of the unconfined compressive strength of the normal strength concrete adhered to AASHTO T22 and ASTM C39 specifications. The load applied to the cylinders remained within 565 lb/s to 1414 lb/s, with the target load being 1272 lb/s. The f'_c of each cylinder can be calculated using Equation 21 when the surface area of the top of the cylinder and the load at which the cylinder failed are known.

$$\boldsymbol{f'_c = \frac{load\ at\ failure}{\frac{\pi}{4}d^2}} \tag{21}$$

Table 4.2: Normal strength concrete f'_c values

Cylinder	Days cured	Avg. Strength (MPa)	Avg. Strength (psi)
1	7	30.1	4370
2	7		
3	7		
4	15	33.9	4910
5	15		
6	15		
7	19	36.1	5230
8	19		
9	19		
10	28	39.2	5680
11	28		

The average of three 6 in x 12 in cylinder breaks, compiled in Table 4.2, gives the f'_c of the concrete at 7 days, and at block testing days. The density of the normal strength concrete was calculated to be 2412 kg/m^3 (150.6 lb/ft^3). Since the strengths measured from the 7 day cylinder tests exceeded the target 28 day compressive strength of 24.8-27.6 MPa (3600-4000 psi), preparations were made to shoot the blocks earlier than 28 days after the pour. The compressive strengths of the blocks on test days ranged from 4914 psi to 5230 psi, while the 28 day strengths are only included as an additional reference point.

4.2.2. Block 1. The photos in Figure 4.3 indicate that Projectile 6 impacted Block 1 near the center. The photo taken of the broken interior concrete, on the left in Figure 4.3, shows the deepest point of the crater near in the bottom right quarter of the block. The photo of the back face shows the assumed impact point to be almost perfectly centered. The rest of the concrete that formed the block shattered into pieces too small to easily recover and piece back together, a result that carries through all of the shots where the projectile does not impact the block significantly off-center. The crater depth at the impact point, measured from the original location of the front face, equals 0.48 m (18.75 in.). Block 1 has a remaining concrete volume of 0.042 m^3 (1.489 ft^3).

Figure 4.3: Block 1, interior and back face views after impact.

4.2.3. Block 2. The junction of the fractures on Block 2 show that Projectile 7 struck the block along the centerline, approximately 5.1 cm (2 in.) below center. The impact broke the back of the block into five pieces. In Figure 4.4, the uneven ground results in the illusion of a wide central fracture. However, the gridlines on the block do not indicate any substantial concrete loss around the central fracture. The photo on the right in Figure 4.4 shows no obvious crater formed by the projectile impact. Instead, the remaining concrete has irregular fracture patterns, while the triangular shaped hole in the middle of the block indicates the axis of impact. At the impact location, depth from the original front face to the intact material equals 0.58 m (23 in.). Block 2 has a remaining concrete volume of 0.041 m^3 (1.439 ft^3).

After the projectile impact, Block 2 appeared to have failed such that the center of mass of the block remained in place, while the fractured pieces of concrete scattered outward. The remaining concrete in the expected center or mass position has a cone shape. Figure 4.5 shows the concrete block pieces after the impact, looking towards the former position of the front block face. The two pieces in the picture with gridlines are part of the back face of the block. Also shown in Figure 4.5 is the approximate cone height of 21.5 cm (8.5 in.).

Figure 4.4: Block 2, back face and interior views after impact.

4.2.4. Block 3. The back face of Block 3, shown in the left photo of Figure 4.6 suggests a slightly high, 7.6-10.2 cm (3-4 in.) right of center impact location. A triangular hole –approximately 10.2 cm (4 in.) wide on the back face, reveals the axis of impact. In addition to the larger area of missing concrete, the block also has a smaller hole, directly below the center of the block, which may have also spalled off during the impact. The top view of the block shows a more typical crater shape, with more concrete removed along the axis of impact, and less removed on the edges of the block. The crater depth at the impact point equals 0.58 m (23 in.). Block 3 has a remaining concrete volume of 0.034 m^3 (1.193 ft^3).

Figure 4.5: Block 2, concrete scatter after impact.

4.2.5. Block 4. Block 4 does not have a section on the back face where spalling occurred to indicate the impact point of Projectile 9. However, judging from the crater shown in Figure 4.7, the projectile impacted the block very close to the center of the block. The crater looks to be approximately 15.2 cm (6 in.) in diameter. The crater boundary has a greater thickness of concrete than the areas inside or outside of the 15.2 cm (6 in.) crater. The depth of the crater at the impact point equals 0.53 m (20.75 in.). Block 4 has a remaining concrete volume of 0.044 m^3 (1.543 ft^3).

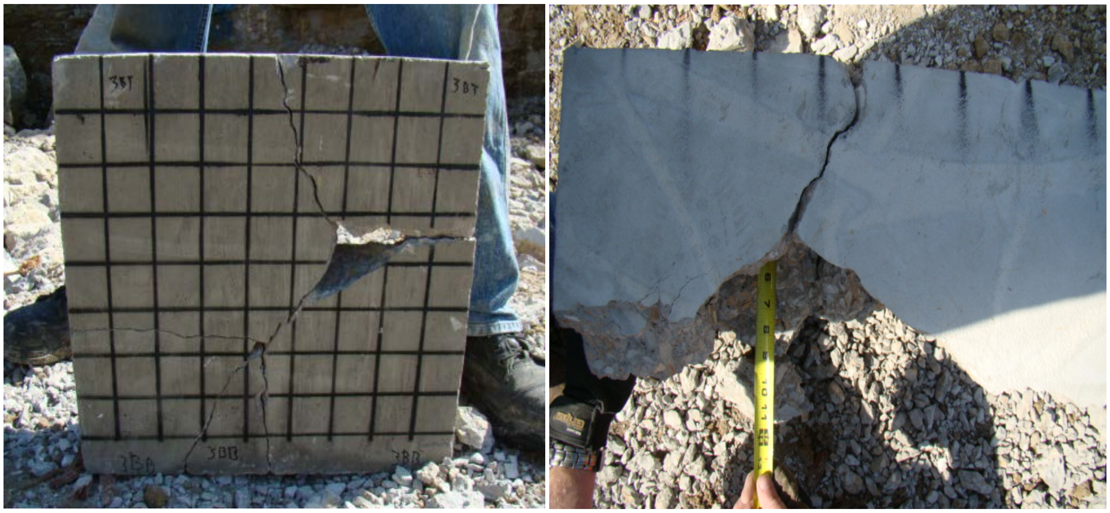

Figure 4.6: Block 3, back and top faces after impact.

Figure 4.7: Block 4, back face and interior views, after impact.

4.2.6. Block 5. Projectile 10 struck Block 5 approximately 7.62 cm (3 in.) below center, as shown in Figure 4.8. In Figure 4.8, the upside-down orientation of the block results in the bottom of the block located at the top of the photo. The upside-down orientation prevented the block from falling over while being photographed. The off-center impact caused the front face of the block to break into only two pieces, instead of the many smaller pieces observed in the shots thus far. The back half of the block broke into five pieces despite the lack of shattered concrete on the front half of Block 5. The off center impact resulted in a shallower crater depth of 0.34 m (13.5 in.). Due to the large size of the rear face of the block, the remaining volume of concrete could not be determined with the Archimedes method using the available containers.

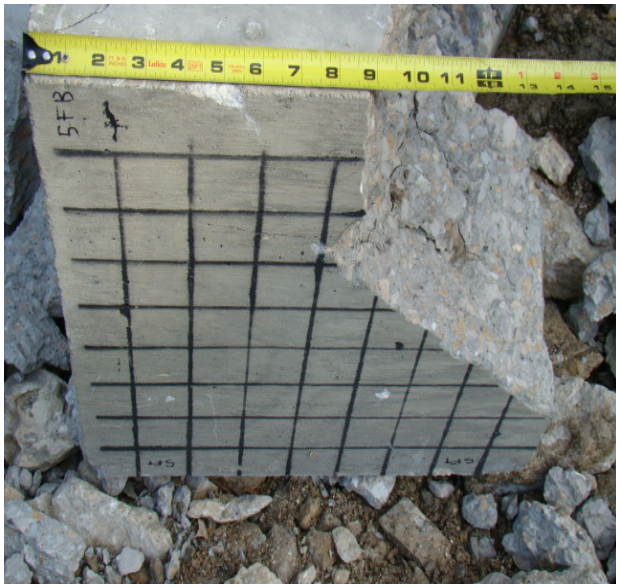

Figure 4.8: Block 5, front face after impact.

4.2.7. Block 6. Projectile 11 hit block 6 just below and left of center as shown in Figure 4.9. Again, a small piece of concrete is missing where the four fractures join, representing the only section of concrete that spalled. The interior of the block, shown on the right side of Figure 9 does not show a clear crater. Instead, above the impact, more material has been broken than the material present below the impact point. Above the impact point, roughly 20.3 cm (8 in.) of concrete remains, while below the impact point nearly 30.5 cm (12 in.) of concrete remains. The depth of the crater at the impact point equals 0.50 m (19.88 in.). Block 6 has a remaining concrete volume of 0.038 m^3 (1.354 ft^3).

Figure 4.9: Block 6, back face and interior views after impact.

4.2.8. Block 7. The fractures on the back face of Block 7, pictured in Figure 4.10, show that Projectile 12 struck the block just to the left of the center square. In addition to the small piece of concrete missing from the back face along the axis of impact, two additional pieces of concrete fractured off the back face of Block 7 from the right and left sides, along the horizontal fracture lines. The impact formed an irregular diamond shaped crater in the block, where more material fractured off around the axis of impact. Looking at the interior view, more concrete appears to have fractured off along the horizontal fracture line than along the vertical fracture line. The depth of the crater at the impact point equals 0.53 m (20.75 in.). Block 7 has a remaining concrete volume of 0.040 m^3 (1.437 ft^3).

Several pieces of the front face of Block 7, recovered after the shot, are pictured in Figure 4.11. The recovered concrete pieces, when placed together, make up the entire top of the front face. The fractured surfaces of the pieces nearest the original center of the block have a curved fracture pattern. The curved fracture surface reveals a material failure which looks like it occurred circularly around the impact point on the block.

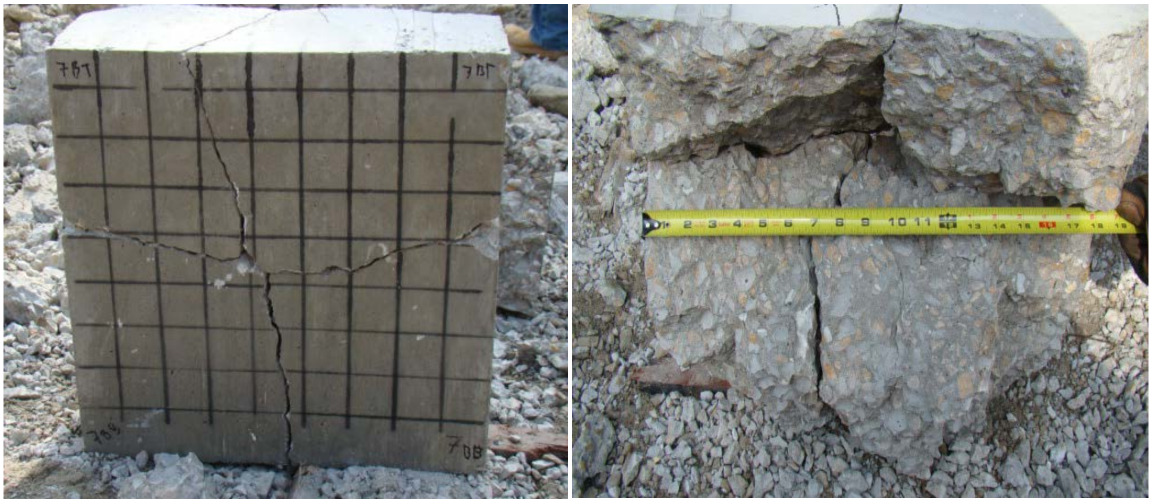

Figure 4.10: Block 7, back face and interior views after impact.

4.2.9. Block 8. Looking only at the single fracture line on the back face of Block 8 makes determining the impact point of Projectile 13 difficult. However, the interior view of the block suggests that the projectile hit the block roughly 2.5 cm (1 in.) right of, and 7.62 cm (3 in.) above center. As seen in Figure 4.12, Block 8 also experienced a failure where the center of mass of the block remained in its original location, while the material around it broke away, leaving a cone of concrete. From Figure 4.13, the height of the concrete cone can be determined to be right at 22.9 cm (9 in.), which amounts to half the original height of the block. Also shown in Figure 4.13 are pieces from the bottom of the front face. The fracture pattern suggests material failure in a circular pattern around the point of impact. The depth of the crater at the impact point equals 0.43 m (16.88 in.). Due to the large size of one of the rear face pieces, the remaining volume could not be measured with the available equipment.

Figure 4.11: Block 7, front face pieces recovered after impact.

4.2.10. Block 9. The damage to the front face of Block 9 points toward an impact in the bottom, right quadrant of the block. The low, off-center impact created a shallower crater than seen in the other tests, with a depth of 0.21 m (8.13 in.). Figure 4.14 shows the diameter of the crater to be approximately 30.5 cm (12 in.). The cavity formed by the projectile looks like a 'typical' crater shape- roughly hemispherical. The back face of Block 9 did not break into multiple pieces, and no spalling could be observed on any of the sides or back of the block. The size of the remaining pieces of concrete exceeded the volume of the available containers for the Archimedes method, so the volume of Block 9 could not be determined.

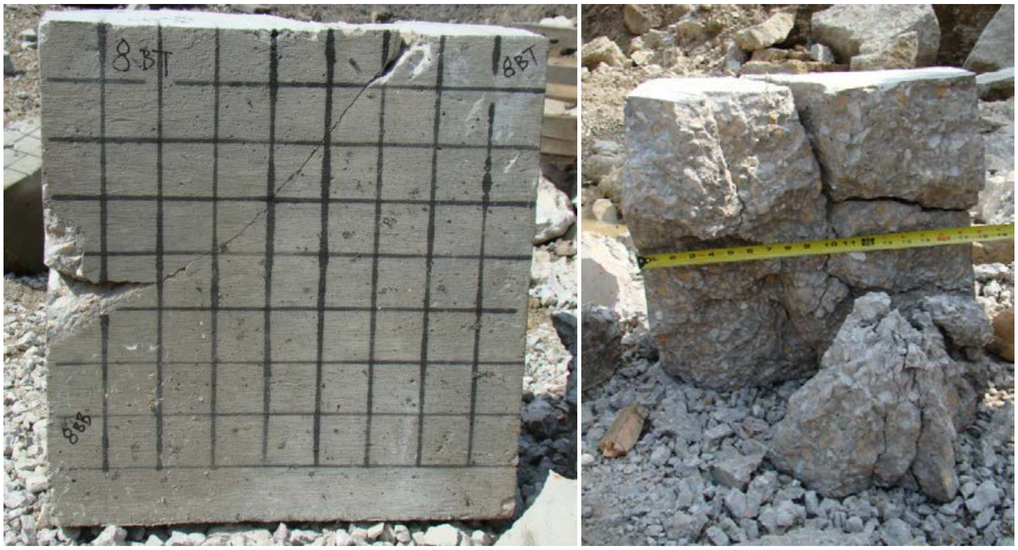

Figure 4.12: Block 8, back face and interior views after impact.

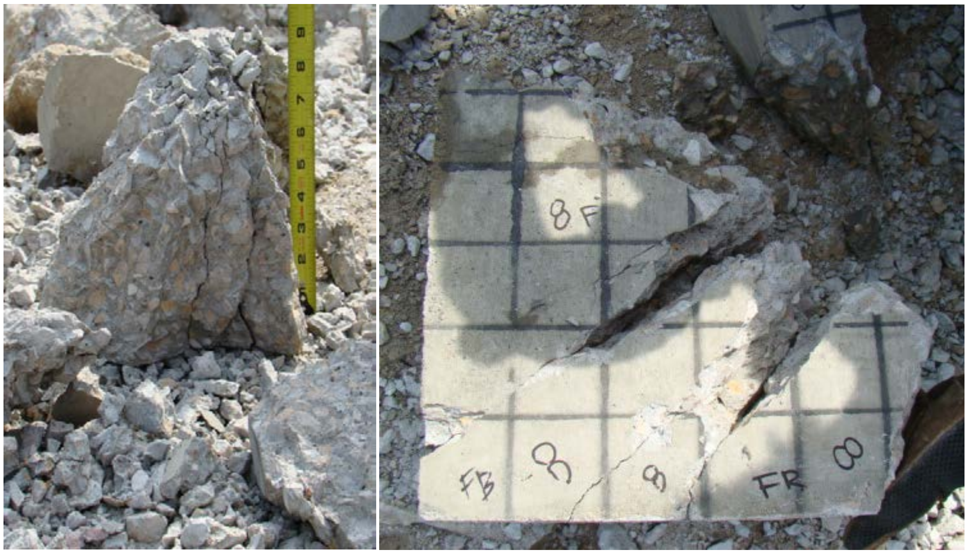

Figure 4.13: Block 8, center and recovered front pieces after impact.

Figure 4.14: Block 9, front face after impact.

4.2.11. Block 10. Projectile 15 struck Block 10 low, and probably very near the vertical centerline of the block. The low impact caused a shallower crater to be formed, similar to Block 9. The lack of fracturing of the block resulted in pieces too large to measure the volume of, using the available containers and equipment. Upon recovering some of the larger pieces of concrete and placing them back together, a crater with a relatively circular shape appears. Using the painted grid as a reference, Figure 4.15 shows that crater has a diameter of 20.3-22.9 cm (8-9 in.). One small piece of concrete, about 2.5 cm (1 in.) in diameter, and very thin, broke off the back of the block. The location of this missing piece of concrete did not appear to be opposite the impact, with its placement on the upper, left-hand side of the back block face. On the front face of the block, there are two small pieces of concrete chipped off, seen as the lighter-colored areas in Figure 4.15, and are most likely from small pieces of shrapnel generated by the blast. The two small divets are not from the impact of the main projectile and are not considered in the analysis. The brown spots seen on the front face of Block 10 are mud splatter, kicked up from the blast.

Since the impact on Block 10 occurred so far off center and resulted in a much shallower crater depth than the previous tests, the results from Block 10 were omitted from the data analysis.

Figure 4.15: Block 10, front face after impact

4.3. HIGH STRENGTH CONCRETE TESTS

4.3.1. Concrete Compressive Strength. The high strength concrete cylinder tests also followed AASHTO T22 and ASTM C39 guidelines, with a target loading rate of 1272 lb/s. The unconfined compressive strengths of the high strength concrete cylinders, calculated using Equation 21 from Section 4.2.1 are shown below in Table 4.3. The 28 day average cylinder strengths exceed the 41.4 MPa (6000 psi) minimum strength to be considered high strength concrete. The density of the concrete, calculated from the cylinders, equaled 2510 kg/m^3 (4231 lb/yd^3).

Table 4.3: High strength concrete f'_c values

Cylinder	Days cured	Avg. Strength (MPa)	Avg. Strength (psi)
5	7	32.6	4725
6	7		
9	7		
4	28	46.0	6670
7	28		
8	28		

4.3.2. Block 11. Projectile 16 hit Block 11 less than 5.1 cm (2 in.) to the right of the center of the block. The volume of concrete that did not completely shatter from the impact broke into four pieces, as shown in Figure 4.16. Two pieces spalled off the back of the block, including a triangular piece of concrete along the assumed axis of impact, and a smaller piece above and to the left of the larger, triangular piece. The concrete broke away from the block in an undefined pattern. However, more concrete seems to have been removed from the block along the fracture lines than the other areas of the block. The depth of the crater at the impact point equals 0.49 m (19.38 in.). Block 11 has a remaining concrete volume of 0.038 m^3 (1.350 ft^3).

Figure 4.16: Block 11, back face and interior views after impact

4.3.3. Block 12. Projectile 17 hit Block 12 very close to the center; Figure 4.17 shows the missing area on the back of the block, which includes the top gridline of the center block. The impact created a hole stretching through the entire thickness of the block. However, after the shot, nothing behind the original block location suggested that the projectile exited the rear face of the block. Looking at the interior of Block 12, it can be clearly seen that the amount of concrete removed from the block is greatest near the impact point. The measured depth of the crater at the impact point equals the original thickness of the block- 0.58 m (23 in.). Block 12 has a remaining concrete volume of 0.035 m^3 (1.223 ft^3).

4.3.4. Block 13. As seen in Figure 4.18, Block 13 has a different fracture pattern on the rear face than what has occurred in the previous twelve shots. Less than half of the concrete in the central square of the block remains, indicating that the projectile struck the block very close to center. The impact caused a 5.1 cm (2 in) strip of concrete stretching from the center to the top of the block along the vertical centerline to break away from the block. The depth of the crater at the impact point equals 0.58 m (23 in.). Block 13 has a remaining concrete volume of 0.040 m^3 (1.413 ft^3).

Figure 4.17: Block 12, back face and interior views after impact

4.3.5. Block 14. Looking at the rear face of Block 14, pictured in Figure 4.19, it appears that the projectile struck the block just below center. Some of the concrete within the grid block just below the center of the block appears to have spalled off of the block. The rear part of the block broke into six pieces, with one piece resembling a long, skinny rectangle, much like the missing piece from Block 13. The view of the interior of Block 14, also pictured in Figure 4.19, shows larger amounts of concrete missing near the impact point and on the corners of the block. The material left seems to show a roughly hemispherical crater, about 17.8 cm (7 in.) in diameter at the center of the block. The depth of the crater at the impact point equals 0.46 m (18.0 in.). Block 14 has a remaining concrete volume of 0.044 m^3 (1.560 ft^3).

Figure 4.18: Block 13, back face after impact

Figure 4.19: Block 14, back face and interior views after impact

4.3.6. Block 15. The four fractures on the back of Block 15 meet at the top left corner of the center square, indicating that Projectile 20 struck the block very close to center. The size of the hole in the rear face opposite the assumed impact point is smaller than the previous high strength blocks. Looking at the interior of the block, in Figure 4.20, a small crater shape in the bottom half of the block can be seen. This small crater on the interior of the block does not appear to be centered on the axis of impact. Instead, the crater occupies the bottom central part of the block, with the top of the crater in line with the impact point. The concrete did not fracture away from the block evenly, as shown by the larger amount of concrete remaining directly above the small crater. The depth of the crater at the impact point equals 0.49 m (19.38 in.). Block 15 has a remaining concrete volume of 0.041 m^3 (1.442 ft^3).

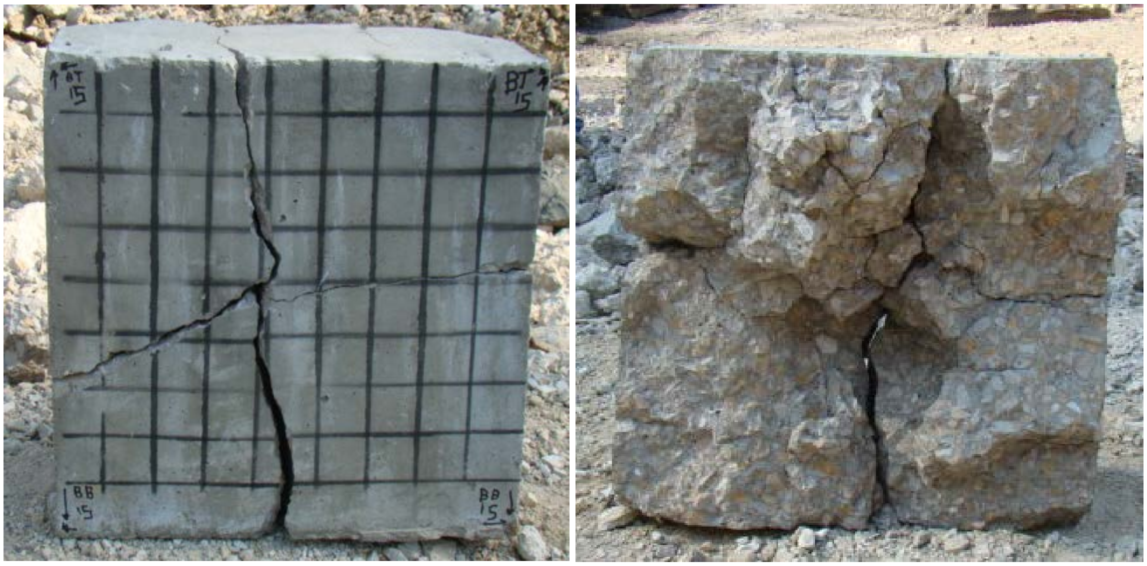

Figure 4.20: Block 15, back face and interior views after impact

4.3.7. Block 16. After being struck by Projectile 21, Block 16 broke into 5 pieces, as shown in Figure 4.21. The junction of the fractures on the rear face point toward an impact located approximately 2.5 cm (1 in.) below and 5.1 cm (2 in.) to the left of center.

The impact of the projectile did not cause a large piece on the rear face to spall off of the block, unlike several of the previous high strength tests. Looking at the interior of the block, no obvious crater is present. However, more material appears to have broken away from the block along the fracture lines and at the corners of the block. The depth of the crater at the impact point equals 0.50 m (19.5 in.). Block 16 has a remaining concrete volume of 0.041 m^3 (1.442 ft^3).

Figure 4.21: Block 16, back face and interior views after impact

4.3.8. Block 17. Figure 4.22 clearly shows that Projectile 22 did not hit Block 17 on or very close to the center. The off-center impact broke the block into two unequal pieces. The interior view of the block reveals an uneven fracture pattern, with no clearly defined crater from the impact. The approximate impact location of the projectile does correspond to a slightly deeper area above and to the right of center in the photo on the right side of Figure 4.22. More concrete also fractured away from the bottom corners of the block than from the central and upper portions of the block. The depth of the fractured material, measured from the original front face, at the impact point equals 0.42

m (16.38 in.). Due to the large size of the rear face pieces, the remaining volume of concrete of Block 17 could not be measured with the available setup.

4.3.9. Block 18. Looking at the back face of Block 18 in Figure 4.23, it appears that the projectile struck the block just below center. The impact broke the block into five pieces, four pieces approximately one quarter of the size of the back face, and one smaller, unrecovered piece. The missing piece left a rectangular hole, approximately 20.3 cm (8 in.) tall and 5.1 cm (2 in.) wide. This smaller, missing piece looks very similar to pieces from Blocks 13 and 14. The interior view of Block 18 shows no clearly defined crater near the assumed impact point. Instead, the right side of the block has a greater volume of intact concrete than the left side, with the central vertical fracture acting as the dividing line. On the left side of the block, more concrete has fractured away from the block along the fracture line, as seen in several of the previous high strength concrete blocks. The depth of the crater at the impact point equals 0.58 m (23 in.). Block 18 has a remaining concrete volume of 0.041 m^3 (1.462 ft^3).

Figure 4.22: Block 17, back face and interior views after impact

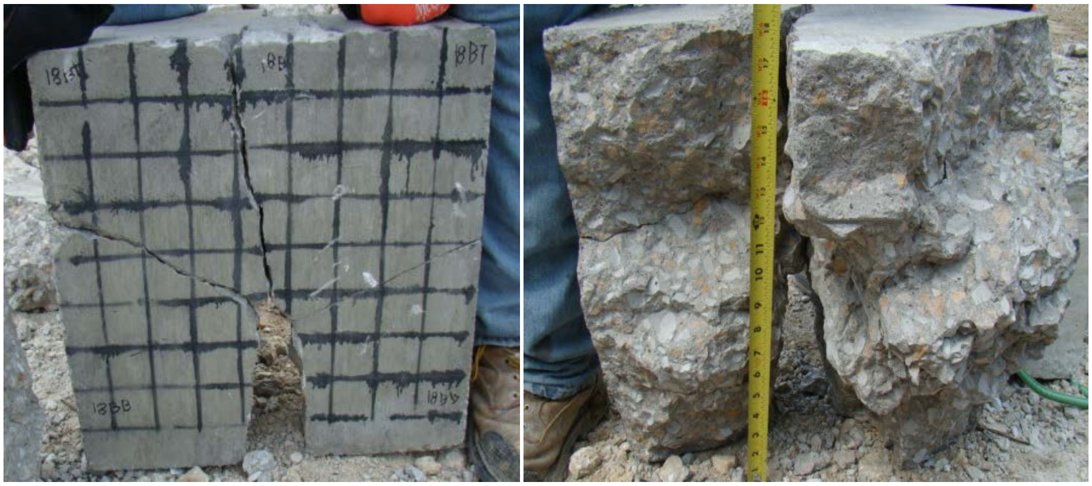

Figure 4.23: Block 18, back face and interior views after impact

4.3.10. Block 19. Projectile 24 appears to have struck Block 19 5.1 cm (2 in.) above and 2.5 cm (1 in.) right of center. The photo on the left side of Figure 4.24 shows that the block split into four pieces, with the fracture lines meeting at the impact point. There is a hole on the back face of the block, approximately 5.1 cm (2 in.) at its widest point. Two other pieces of concrete are also missing from the back face, located where the main fractures meet the left and top sides of the block. The view of the interior of the block shows that more concrete broke away from the block around the impact point and near the corners of the block. The diameter of the crater around the axis of impact ranges from approximately 15.2 cm (6 in.) at the interior face to 5.1 cm (2 in.) at the rear face of the block. Both photos in Figure 4.24 clearly show a hole that extends through the entirety of the remaining concrete. The depth of the crater at the impact point equals 0.58 m (23 in.). Block 19 has a remaining concrete volume of 0.033 m^3 (1.150 ft^3).

4.3.11. Block 20. Block 20 appears to have been hit 2.5 cm (1 in.) right of center. The center square on the grid has been partially destroyed by concrete spalling off the back face of the block. The material spalled off the back of the block, leaving a triangular hole roughly 7.62 cm (3 in.) wide at the base and 7.62 cm (3 in.) tall. The projectile impact broke the block into four pieces, and the top two pieces are much larger than the bottom two pieces. The interior view of the block, pictured on the right side of Figure

4.25, does not show a clear crater-like shape, nor does it show that more material broke away from the block along the main fracture lines. While the rear face has a hole where material spalled off of the block, the interior view plainly shows that the projectile impact did not cause a hole to form through the entire length of the block. Block 20 has a remaining concrete volume of 0.046 m^3 (1.616 ft^3), and the depth of the crater at the impact point equals 0.34 m (13.5 in.).

Figure 4.24: Block 19, back face and interior views after impact

4.4. INSTRUMENTATION DATA

The only instrumentation used during testing Blocks 1-10 consisted of a high speed camera, while shots 11-20 had both the high speed camera and oscilloscope setup to record projectile velocities. The velocities, determined with the software package associated with the camera, for the projectiles that struck Blocks 1-10 are tabulated in Table 4.4. The velocities collected from the oscilloscope setup, along with the differences between the two methods of measurement, where applicable, are also tabulated in Table 4.4. Gray blocks indicate values not measured experimentally.

In Table 4.4, in addition to the oscilloscope values for Blocks 1-10, which were not taken, the camera and oscilloscope velocities for Block 16 are also missing. During the shot on Block 16, the oscilloscope failed to trigger, and the camera triggered too early to capture the event. For Blocks 12, 13, 14, and 18, the camera and oscilloscope velocities are in good agreement with each other. For the rest of the high strength blocks, there are significant differences in the velocities measured with the camera and oscilloscope. These differences will be addressed in the Discussion section, Section 5.

Figure 4.25: Block 20, back face and interior views after impact

4.5. COMPILATION OF IMPACT DATA

For easy reference, the initial flyer mass, estimated final projectile mass, impact location, camera velocity, crater depth, and remaining volume of concrete for Blocks 1-20 are tabulated below in Table 4.5 and Table 4.6. Instead of using the oscilloscope velocities, the more consistent camera velocities are used in the data compilation tables and the discussion section. As with Table 6, gray blocks indicate values not measured experimentally.

Table 4.4: Compiled camera and oscilloscope velocities

Block	Projectile	Camera velocity (m/s)	Camera velocity (ft/s)	O-scope velocity (m/s)	O-scope velocity (ft/s)	ΔV, (m/s)	ΔV, (ft/s)
1	6	1317	4320				
2	7	1350	4428				
3	8	1306	4285				
4	9	1303	4274				
5	10	1321	4333				
6	11	1303	4275				
7	12	1284	4213				
8	13	1345	4413				
9	14	1302	4273				
10	15	1314	4312				
11	16	1223	4014	879	2885	344	1129
12	17	1302	4273	1270	4167	32	106
13	18	1283	4209	1270	4167	13	42
14	19	1249	4099	1203	3947	46	152
15	20	1219	3999	737	2419	481	1580
16	21						
17	22	1242	4074	914	3000	327	1074
18	23	1302	4273	1203	3947	99	326
19	24	1273	4178	1039	3409	234	769
20	25	1284	4213	1089	3571	196	642

4.6. RECOVERED PROJECTILES

During testing of the normal strength concrete blocks, the researchers did not recover any projectiles, despite searching the test site. However, during the high strength concrete testing phase, the researchers found pieces of seven projectiles. Three of the projectiles can be matched with the blocks they impacted. The blocks that the other four projectiles struck cannot be determined since the projectiles were not recovered immediately after each test. The projectile pieces did not land at a consistent area relative to the original block location. Recovered projectile locations ranged from less than 0.30 m (1 ft) to approximately 12.2 m (40 ft) from the original block locations, with projectile pieces landing in front of, behind, to the left of, and to the right of the original block location. Photos of the recovered projectiles are shown in Figures 4.26-4.28.

Table 4.5: Compilation of Normal Strength Concrete Impact Data

Block	Flyer	Init. Flyer Wt. (kg)	Final Est. Flyer Wt. (kg)	V_0 (m/s)	Depth at impact (m)	Remaining Volume (m^3)
1	6	0.449	0.372	1317	0.48	0.042
2	7	0.436	0.359	1350	0.58	0.041
3	8	0.447	0.370	1306	0.58	0.034
4	9	0.440	0.363	1303	0.53	0.044
5	10	0.452	0.375	1321	0.34	
6	11	0.452	0.375	1303	0.50	0.038
7	12	0.440	0.363	1284	0.53	0.040
8	13	0.445	0.368	1345	0.43	
9	14	0.445	0.368	1302	0.21	
10	15	0.447	0.370	1314		
			Averages:	1314	0.46	0.040

Table 4.6: Compilation of High Strength Concrete Impact Data

Block	Flyer	Init. Flyer Wt. (kg)	Final Est. Flyer Wt. (kg)	V_0 (m/s)	Depth at impact (m)	Remaining Volume (m3)
11	16	0.456	0.379	1223	0.49	0.038
12	17	0.456	0.379	1302	0.58	0.035
13	18	0.459	0.382	1283	0.58	0.040
14	19	0.461	0.384	1249	0.46	0.044
15	20	0.456	0.379	1219	0.49	0.041
16	21	0.459	0.382		0.50	0.041
17	22	0.459	0.382	1242	0.42	
18	23	0.459	0.382	1302	0.58	0.041
19	24	0.459	0.382	1273	0.58	0.033
20	25	0.459	0.382	1284	0.34	0.046
			Averages:	1264	0.50	0.040

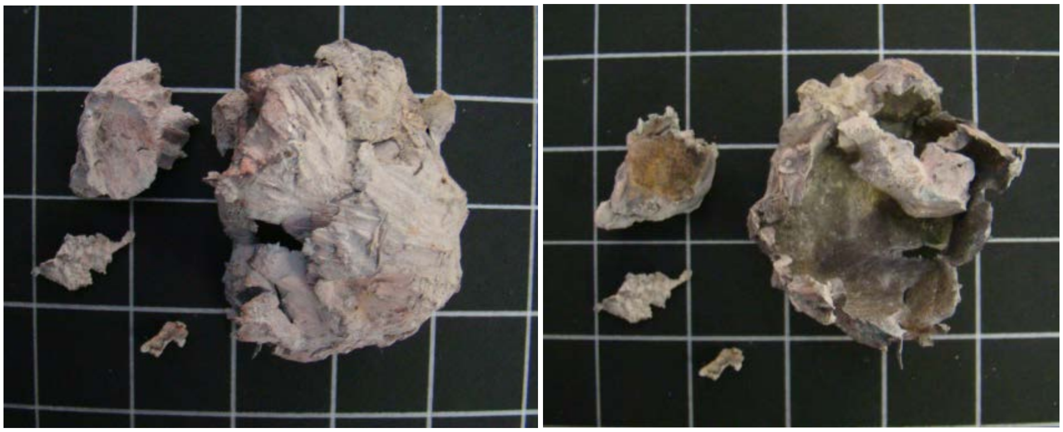

Figure 4.26: Recovered pieces of Projectile 23

Figure 4.27: Recovered piece of Projectile 24

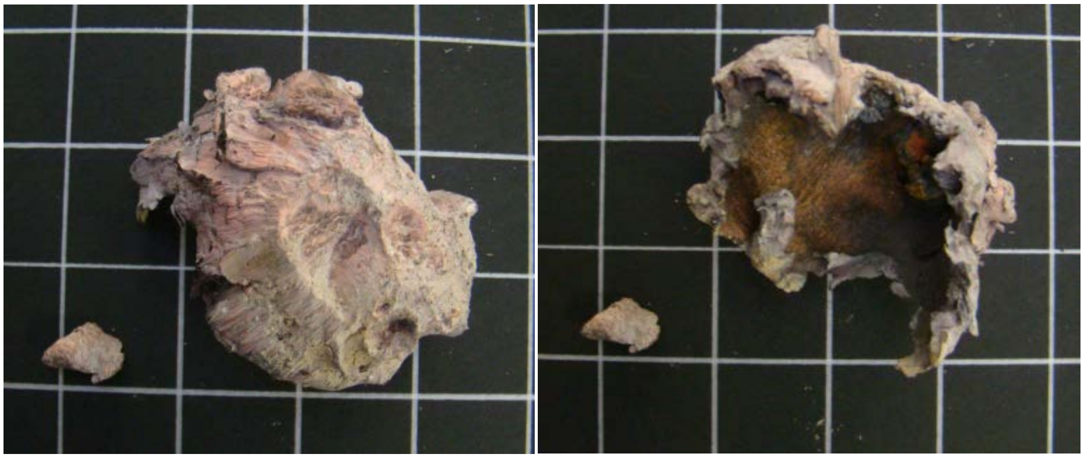

Figure 4.28: Recovered pieces of Projectile 25

Figure 4.29: Recovered pieces of unknown projectiles

5. DISCUSSION

5.1. HUGONIOT CALCULATIONS

Throughout Section 5, the Hugoniot calculations and shockwave analysis are based on the Hugoniot calculations found in Reference (13), and should be considered to be a simplified analysis. These simplified calculations do not take into account energy removed from the system when pieces of concrete fracture off and move away from the block.

5.1.1. Projectile Impact on a Normal Strength Concrete Block. Assuming that the impact of the projectile on the block produces a hemispherical shockwave and that the reflections off the sides and back of the block are also hemispherical yields a shockwave pattern like that shown in Figure 5.1. The central cross-section of a normal strength block has three different colors of shockwave, with the black lines corresponding to the original shockwave and blue to the rarefactions. The calculations used to determine shock velocities are addressed in Sections 5.1.1.1, 5.1.1.2, and 5.1.1.3. The rarefactions originating from the front corners and the sides of the block do not have enough time to catch the original shockwave, but are catching up as expected, since a rarefaction moves more quickly through a shocked (denser) material than the original shockwave moves.

5.1.1.1 Initial Shockwave Caused by Projectile Impact. Using the Hugoniot equations of state, the shock velocities and pressures created within the target by the projectile impact can be estimated. At the point and time of impact, both the pressure and particle velocity in the projectile and target must be equal (13). With this relationship in mind, and knowing the initial conditions of both the projectile and target, the resulting particle velocity can be calculated by equating the equations for the left-going and right-going shocks, given in Equation 22.

$$\boldsymbol{\rho_0 C_0(u_0 - u_1) + \rho_0 s(u_0 - u_1)^2 = \rho_0 C_0(u_1 - u_0) + \rho_0 s(u_1 - u_0)^2} \tag{22}$$

When the right-going projectile strikes the stationary target, a right-going shock in the target and a left-going shock in the projectile are created. The left-side of Equation 22, describes the left-going shock in the projectile, and the right-side of Equation

22describes the right-going shock in the target. The initial values used in Equation 22 to calculate the shocked particle velocity, u_1, are shown below in Table 4. The * next to a value indicates values taken from reference (13), while the † next to a value indicates values taken from reference (14), and values with no symbol are experimental values. Solving Equation 22, with the values given in Table 9 yields a shocked particle velocity of 1.04 km/s (3412 ft/s). Using u_1=1.04 km/s along with the other initial values in Equation 22 gives a compressive pressure within the block of 10.65 GPa.

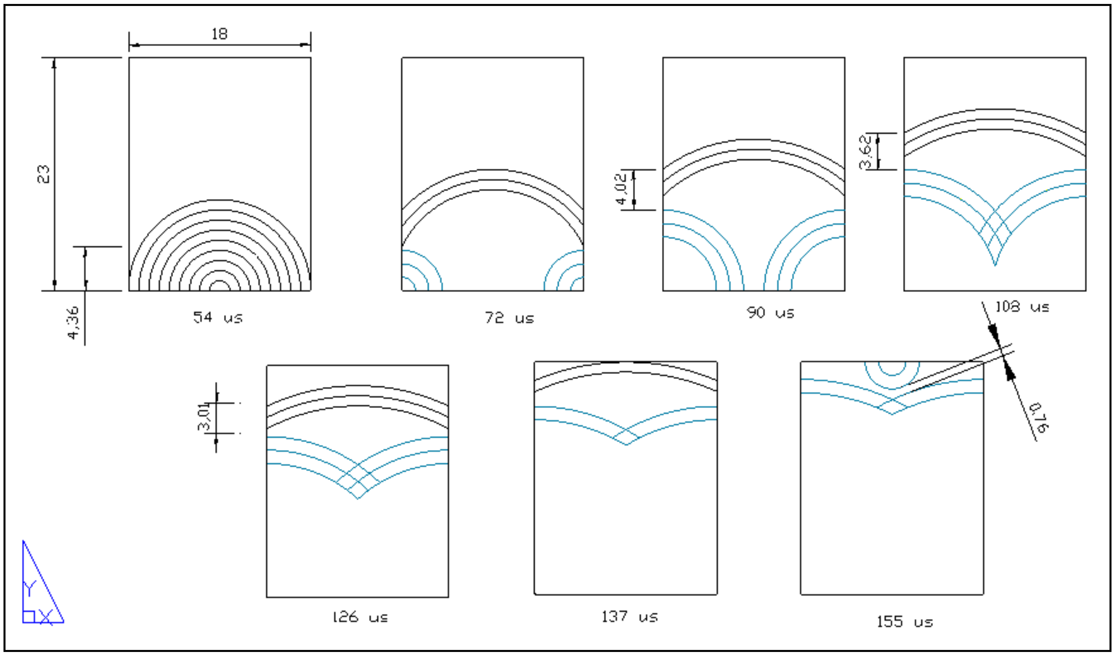

Figure 5.1: Shockwave interactions from centered impact (inches)
Black lines: original shockwave, Blue lines: rarefaction

Now that the shocked particle velocity has been calculated, the shock velocity, (U_1), of the shock traveling through the concrete block can be calculated using Equation 23. (13)

$$\boldsymbol{U_1 = C_0 + su_1} \tag{23}$$

The calculated shock velocity for the shockwave generated by the projectile impact equals 4.25 km/s (13,944 ft/s). For a centered impact, the shockwave will reach the left and right sides of the block in 54 µs, and will reach the rear face at 137 µs.

Table 5.1: Initial Values used in Equation 22

	Copper Projectile	Concrete Target	Units
Unshocked density (ρ_0)	8.930*	2.41	g/cc
Bulk Sound Speed (C_0)	3.940*	2.906†	km/s
Slope of U-u Hugoniot	1.489*	1.289†	N/A
Unshocked particle velocity (u_0)	1.315	0	km/s

5.1.1.2 Reflection of Shockwave off Side/Back of Block. When a shockwave reaches a free surface, such as the sides and back of the concrete block, a rarefaction wave is created. The rarefaction wave moves into the shocked material in the opposite direction of the original shockwave. Since the original shock and the rarefaction are traveling in opposite directions within the same material, and the magnitude of the pressure at the location where they meet must be equal, the Hugoniots are mirror images of each other. If the mirror image P-u Hugoniots are plotted, the plot shows that the resulting particle velocity following the rarefaction equals $2u_1$.The pressures and particle velocities for a shock and rarefaction interaction are shown in Figure 5.2. (13)

Therefore, the particle velocity following the rarefaction in the normal strength concrete block equals twice the particle velocity calculated in Section 5.1.1.1, which equals2.08 km/s (6824 ft/s). Using the particle velocity of the rarefaction (u_R), and Equation 23, the rarefaction wave velocity (U_R) can be calculated. For the rarefactions generated at the sides and rear of the normal strength block with the initial conditions in Table 5.1, U_R equals 5.59 km/s (18,340 ft/s).

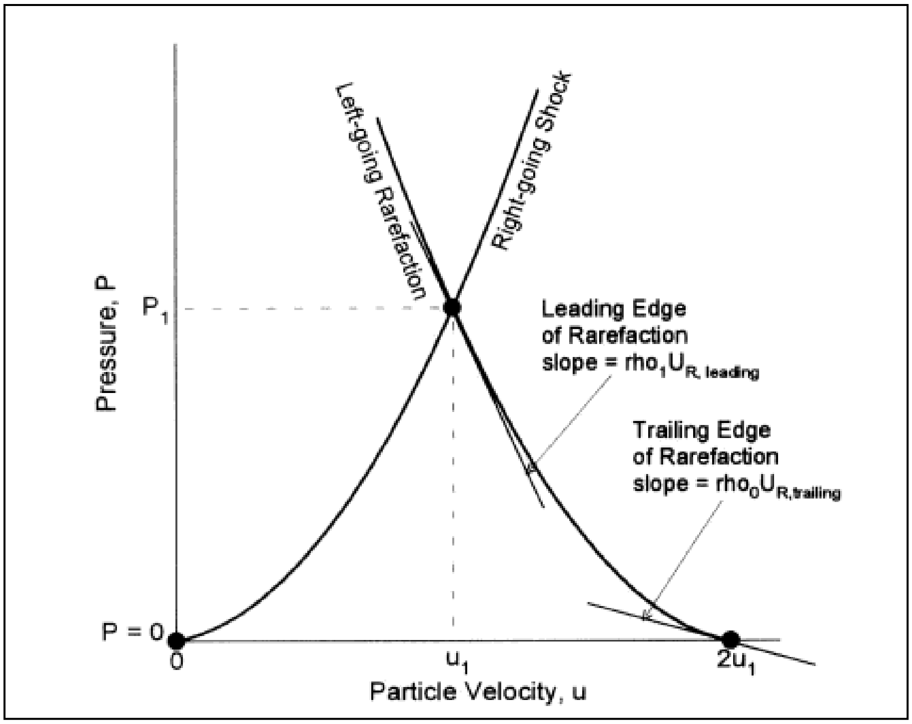

Figure 5.2: Shock-Rarefaction Interaction (13)

5.1.1.3 Interaction of Two Rarefactions. The interaction of the original shock with the left and right sides of the block creates two rarefactions heading in opposite directions. The rarefactions generated at the left and right sides of the block travel through the already compressed material and meet each other at the centerline of the block. The particle and shock velocities of the rarefactions can be calculated using the shocked density (ρ_1), found with Equation 24, and then equating the equations for a left-going and a right going shock, shown in Equation 22. (13)

$$\boldsymbol{\rho_1} = \boldsymbol{\rho_0}\left[\frac{\boldsymbol{U-u_0}}{\boldsymbol{U-u_1}}\right] \tag{24}$$

Using the shockwave velocity of 4.25 km/s calculated from Equation 23, and the initial density and particle velocities from Table 5.1, the shocked density equals 2.96 g/cc. As the rarefactions, also known as release waves, travel through the shocked material, they “release” the pressure in the material, allowing the pressure to drop to zero as shown in Figure 5.2. As the pressure in the material is returns to zero, the shocked density would return to the unshocked density if the material was not damaged by the shockwave,.

Replacing ρ_0 in Equation 24 with 2.96 g/cc, u_0 with 2.08 km/s, and solving for u_1, gives a particle velocity at the rarefaction interaction of 0 km/s. The new particle velocity of 0 km/s seems reasonable since two rarefactions, of equal wave velocity, traveling in opposite directions should negate each other when they meet.

Using the value u_1 = 0 km/s in either side of Equation 22 results in a calculated pressure of -1.38 GPa at the rarefaction interaction. The -1.38 GPa pressure greatly exceeds the tensile strength of the concrete, which would result in a tensile failure where two rarefactions contact each other in the block if the material had not been damaged by the compressive pressures from the original shock.

5.1.2. Projectile Impact on a High Strength Concrete Block. The initial values used for the Hugoniot calculations on the high strength blocks are the same as listed in Table 5.1, except for the concrete unshocked density, ρ_0 = 2.51 g/cc. However, the values used from Reference (14) only address the varying aggregate sizes, and not different compressive strengths on the U-u Hugoniot values. So, the particle and shock velocities may be a less exact estimation than those calculated for the normal strength concrete blocks.

5.1.2.1 Initial Shockwave Caused by Projectile Impact. Using the initial values described in Section 5.1.2 and Equation 22, the shocked particle velocity, u_1, equals 1.047 km/s. Therefore, according to Equation 23, the velocity of the shockwave generated by the projectile impact equals 4.26 km/s (13,976 ft/s). The shockwave velocity through the high strength concrete block slightly exceeds the shockwave velocity in the normal strength block, which follows the trend that shocks travel faster through materials of higher density. The time, with rounding, for the shockwave to reach the rear face of the block is also 137 µs. The short distance from the front to the rear of the block coupled with the small difference of 0.01 km/s (32.8 ft/s) between the shock velocities in the normal and high strength concrete blocks results in arrival times that differ by less than 1 µs. Using u_1=1.047 km/s along with the other initial values in Equation 22 gives a compressive pressure within the block of 10.39 GPa, a slightly lower pressure than within the normal strength concrete blocks.

5.1.2.2 Reflection of Shockwave off Side/Back of Block. Following the same procedure described in Section 5.1.1.2, the velocity of the rarefaction created when the initial shockwave reaches a free surface equals 5.61 km/s (18,406 ft/s). Again, this velocity is only slightly higher than the velocity calculated for the rarefactions in the normal strength block, which may be partially attributed to the lack of Hugoniot data for different compressive strengths of concrete.

Due to the short distance through the block which the initial shock and rarefaction can travel, along with the similar velocities to those within the normal strength block, the rarefactions generated at the front corners of the block will not catch up to the initial shock as shown in Figure 5.1.

5.1.2.3 Interaction of Two Rarefactions. Following the procedure outlined in Section 5.1.1.3, and using Equation 24, the calculated shocked density of the high strength concrete block equals 3.09 g/cc. Using the shocked density, and previously determined rarefaction and shocked particle velocities in Equation 22, the particle velocity at the interaction of two rarefactions equals 0 km/s. Again, $u_1 = 0$ km/s seems to be a reasonable answer for the reason stated in Section 5.1.1.3.

Using $u_1 = 0$ km/s in either side of Equation 22 results in a calculated pressure of 1.35 GPa where the rarefactions meet. The tensile stress of 1.35 GPa exceeds the tensile strength of the concrete, certainly resulting in a tensile failure wherever two rarefactions interact within the block if the material had not already failed due to the large compressive pressures generated by the projectile impact.

5.1.3. Possible Attenuation of the Shockwaves. Since the values used in the Hugoniot calculations assume, for simplicity, that concrete is a homogeneous material the calculated pressures may be different than the actual pressures. The aggregate and mortar within each block have different densities and Hugoniot properties. The calculations performed in previous sections do not account for the reflections and transmissions that occur when the original shockwave contacts an aggregate-paste interface. The many interactions that occur as the shockwave travels through the block most likely alter the shape of the shock front, resulting in a shock front that does not have a perfectly hemispherical shape. The interactions with the paste and aggregate may also lower the particle velocities and pressures within the block, since a shock traveling from a higher impedance material to a lower impedance material has a lower shock pressure at the material interface. The many reflections that occur at the paste-aggregate interfaces may also partially account for the varied fracture patterns seen on the interior faces of the blocks.

5.2. CENTERED VS. OFF-CENTER IMPACT

For a centered impact like the one shown in Figure 5.1 that generates a shock with a velocity of 4.25 km/s (13,944ft/s), the initial shockwave reaches the sides of the block in 54 µs, and reaches the back of the block in 137 µs. If the projectile strikes the block 5.1 cm (2 in.) off center, then the shockwave will still reach the back of the block at 137 µs, but will reach the first side of the block at 41 µs. Given the short depth of the block that the shockwave and rarefactions can travel, the rarefaction will not catch up with the initial shockwaves as shown in Figure 5.1 and Figure 5.3. However, after a 5.1 cm (2 in.) off-center impact, the first rarefaction generated comes very close to catching up with the original shockwave. A projectile striking the block farther off-center would result in a rarefaction that would overtake the original shockwave and begin to attenuate it, lowering the pressure within the block.

Since the original shockwave expands in a hemispherical pattern from the impact point with an increasing radius, the first point on the rear face to be reached will be directly opposite the impact location, as shown graphically in Figure 5.1 and Figure 5.3. Since the rarefaction formed from the interaction of the original shockwave with this point on the rear face will be the first “release point” for the shock pressure, the pressure will be highest at this point in the block. Therefore, the point opposite the impact point will either spall off or fracture due to the compressive pressures associated with the original shock pressure. The graphical representations only represent the shockwave patterns in a cross-section of the block in one plane associated with the expected projectile trajectory. Due to the square cross-section of the block, the original shockwave will reach the sides of the block before it reaches the corners. Since the shockwave travels in a three-dimensional, not a two dimensional, fashion, the shock will reach all four sides of the block at the point closest to the axis of impact. Upon reaching the edges of the block, the pressure will be “released”, and rarefactions with tensile pressures will travel back into the block. When the tensile pressures created exceed the tensile strength of the concrete, assumed to be seven to eleven percent of the magnitude of the compressive strength (15), and the material fractures, or splits, along the plane. The material behavior just described is consistent with the experimental results shown in Section 4, and explains why the fracture locations on the rear face of the block are dependent upon the impact location. It should be noted that while many materials exhibit dynamic strengths that are higher than their measured static strengths, a test to measure the dynamic strength of concrete does not currently exist. So, while the concrete strengths used in this analysis are static, the conclusions drawn from this research would not be significantly affected if the dynamic strength was used for comparison due to the small difference in static vs. dynamic material strengths when compared to the pressures resulting from the projectile impact.

5.3. EXPERIMENTAL VS. PREDICTED PENETRATION

The equations for predicting projectile penetration depth into concrete require all of or a subset of the following variables: concrete compressive strength, projectile weight or mass, caliber radius head (CRH), nose shape, projectile diameter or radius, projectile weight, and striking velocity. The caliber radius head of a projectile describes the head of the projectile in terms of its ballistic length and the radius of curvature of its nose. Larger CRH numbers indicate a more streamlined projectile. (16) The CRH of a projectile, represented by ψ, equals the ogive radius divided by the diameter of the projectile. (17) The nose shape, average nose radius, average weight loss of each projectile determined from the soft recovery projectiles, and the projectile striking velocity, along with the concrete cylinder strengths allow the experimental data to be compared to the predicted values.

Table 5.2 gives the measured penetration depths compared to the results of seven different formulas for Blocks 1-9, with the outliers highlighted. The differences between the measured and predicted penetration depths are also given in percent, where a negative value indicates under-prediction.

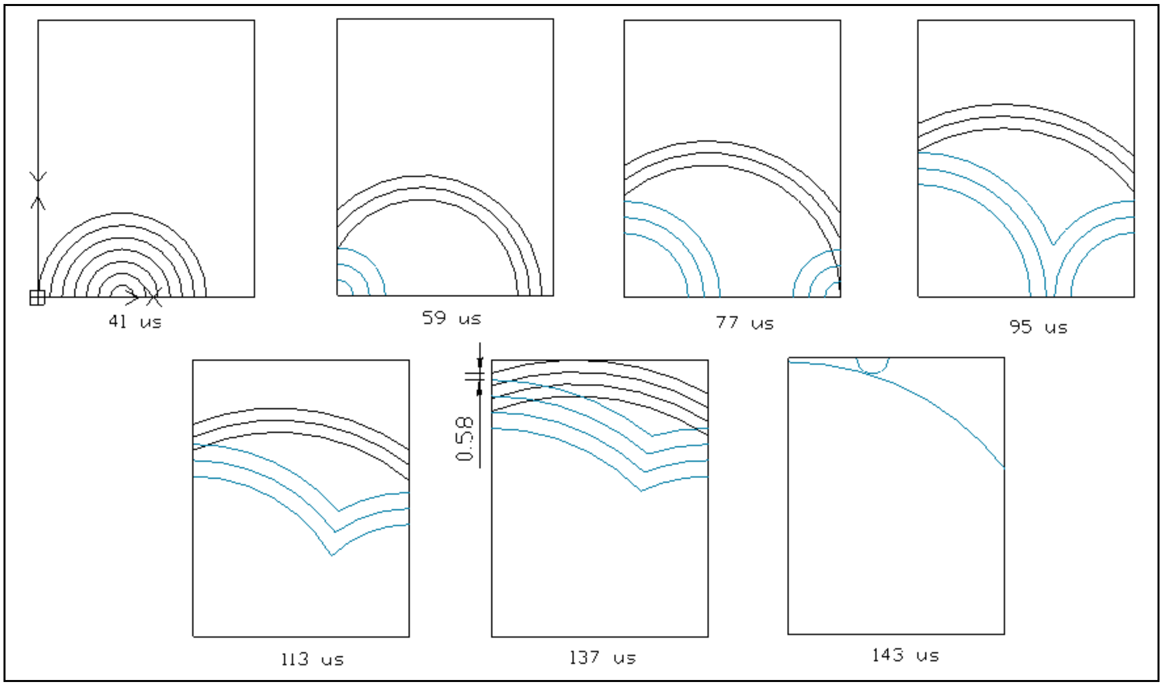

Figure 5.3: Shockwave interactions from off-center impact (inches)
Black lines: original shockwave, Blue lines: rarefaction

The formulas used in Table 5.2 are given in Section 2.1, and all formulas except UFC 3-340-02 were used without modification. The UFC formula requires a modifier based on the projectile material, and Reference (9) does not provide a value for a copper projectile, nor the method used to determine the values given in the text. So, the author chose to use the ratio from the Kar formula between the Young's Modulus of the projectile material and steel (E_{copper}/E_{steel}) as the modifier for the UFC formula. (6) Where the formulas required a factor based on projectile nose shape, the value for a hemispherical projectile was used. A hemispherical projectile has a CRH of 0.5.

In addition to providing the comparison between the measured depths and the predicted values, Table 5.2 also provides the average depths including all the data, and the average of the data, not including the outliers, which are highlighted in yellow. A negative value in a "% dif" row indicates the formula under-predicted the penetration depth, while a positive value indicates an over-prediction. The three outliers for the NSC blocks are Blocks 5 and 9, which had significantly off-center impact points as well as the data for Block 10, were omitted due to the large difference in penetration depth from the other blocks. When comparing the average of all the measured values to the predicted values, the Kar Formula comes closest to the experimental values, under-predicting by 0.006 m (0.24 in.). When comparing the average of the measured values where the outliers are omitted, UFC provides the closest estimate with an under-prediction of 0.045 m (1.77 in.).

Table 5.3 gives the measured penetration depths of Blocks 11-20 and the estimations of penetration depth given by seven different formulas. The only modification to a formula constitutes the Young's Modulus modifier addition to the UFC formula, as previously described. The differences between the measured and predicted penetration depths are also given in percent, where a negative value indicates under-prediction.

Table 5.3 also gives averages with all the data, except for Block 16, which had no striking velocity value, and an average with the outlier (Block 20) omitted. For both an overall average of the data, and the average without the outlier, the Kar formula gave the closest estimates, with under-predictions of 0.064 m (2.5 in.) and 0.087 m (3.4 in.), respectively

5.4. INFLUENCES OF SELECTED FACTORS ON PENETRATION DEPTHS

5.4.1. Effect of Striking Velocity on Penetration Depth. All of the formulas used to predict concrete penetration include the striking velocity of the projectile as a variable. Numerous studies have shown that as the striking velocity increases, so does the penetration depth of the projectile. Figure 5.4 plots the HSC and NSC experimental results, minus the outliers noted in Section 5.3.

Figure 5.4 shows several interesting relationships between the striking velocity of the projectile and the measured depth at the impact point. It should be noted that the projectile velocities measured using the high speed camera, and used to plot the data in Figure 5.4, are not exact values due to the "human error" component associated with using the Phantom software. However, the velocity values, while not exact, should be close to the actual value.

Table 5.2: Experimental vs. Predicted Penetration, NSC

Block	Measured Penetration Depth	Modified Petry Formula	Present Modified NDRC	Amman and Whitney	Whiffen	Kar	Forrestal 1994	UFC 3-340-02
				meter				
1	0.476	0.421	0.777	1.075	0.930	0.465	0.390	0.481
2	0.584	0.410	0.782	1.083	0.924	0.468	0.386	0.484
3	0.584	0.417	0.761	1.053	0.914	0.456	0.386	0.471
4	0.527	0.408	0.744	1.029	0.895	0.446	0.378	0.461
5	0.343	0.424	0.785	1.087	0.939	0.470	0.394	0.486
6	0.505	0.421	0.767	1.062	0.923	0.460	0.390	0.475
7	0.527	0.406	0.726	1.003	0.879	0.436	0.373	0.450
8	0.429	0.419	0.797	1.103	0.944	0.477	0.394	0.493
9	0.206	0.413	0.753	1.041	0.906	0.451	0.383	0.466
Avg (all)	0.465	0.415	0.766	1.060	0.917	0.459	0.386	0.474
% dif (all)		-10.8	64.7	128	97.2	-1.3	-17.0	1.9
Avg w/o outliers	0.519	0.415	0.765	1.058	0.915	0.458	0.385	0.474
% dif		-20.0	48.2	104	76.9	-11.8	-25.8	-8.7

When regression analysis using Minitab ® software is performed on both sets of data, the R^2 results are quite different. The NSC data has an extremely weak correlation between the striking velocity and measured penetration depth with an R^2 value of 0.027, while the HSC data has a moderately strong correlation, demonstrated by the 0.725 R^2 value. The HSC trend-line suggests that for this set of data, an increased striking velocity will result in a deeper measured penetration depth, a characteristic that agrees with the formula predictions. The HSC data points also show that above a certain V_0, the depth is equal to the length of the block, 0.58 m. The two occurrences in the data where there are multiple measured penetration depths for a small velocity range certainly contributed to the small R^2 value. With a wider range of projectile velocities, the NSC data may have had a higher R^2 value.

Table 5.3: Experimental vs. Predicted Penetration, HSC

Block	Measured Penetration Depth	Modified Petry Formula	Present Modified NDRC	Amman and Whitney	Whiffen	Kar	Forrestal 1994	UFC 3-340-02
				meter				
11	0.490	0.415	0.601	0.824	0.741	0.362	0.326	0.372
12	0.580	0.427	0.670	0.922	0.803	0.465	0.327	0.415
13	0.580	0.426	0.656	0.903	0.792	0.456	0.329	0.406
14	0.460	0.424	0.630	0.866	0.771	0.438	0.330	0.390
15	0.490	0.414	0.597	0.818	0.738	0.415	0.325	0.370
16	0.500							
17	0.420	0.420	0.620	0.851	0.760	0.431	0.328	0.384
18	0.580	0.429	0.674	0.928	0.808	0.468	0.329	0.417
19	0.580	0.425	0.648	0.891	0.785	0.450	0.328	0.401
20	0.340	0.427	0.657	0.904	0.793	0.456	0.329	0.407
Avg (all)	0.502	0.423	0.639	0.879	0.777	0.438	0.328	0.396
% dif (all)		-15.7	27.3	75.1	54.8	-12.7	-34.7	-21.1
Avg w/o outliers	0.523	0.423	0.637	0.875	0.775	0.436	0.328	0.394
% dif		-19.1	21.8	67.3	48.2	-16.6	-37.2	-24.7

The data points plotted for, and the trend-line associated with the NSC blocks differ substantially from the HSC data. Despite six of the seven points having striking velocities within 15 m/s (49.2 ft/s) of each other, the measured crater depths range from 0.43 to 0.58 m (16.9 to 23 in.). The regression analysis indicates a very weak correlation between striking velocity and crater depth.

The range of depths for similar velocities exhibited in the NSC data may be due to the principles of fracture mechanics as they relate to concrete. In any heterogeneous material bonds exist between the constituents that make up the material. In this case, the paste (cement, sand, water, flyash) bonds to the aggregate particles. The thin zone surrounding the aggregate particles in concrete differs from the paste further away from the aggregate, and is referred to as the interfacial transition zone (ITZ). When concrete breaks, the fractures begin in the ITZ. (15) The NSC had a larger percentage of aggregate, and therefore aggregate-paste interfaces, than the HSC. The larger amount of aggregate-paste interfaces in the NSC may have allowed the stresses from the impact to distribute in a variety of ways, contributing to the larger amount of scatter in the NSC data.

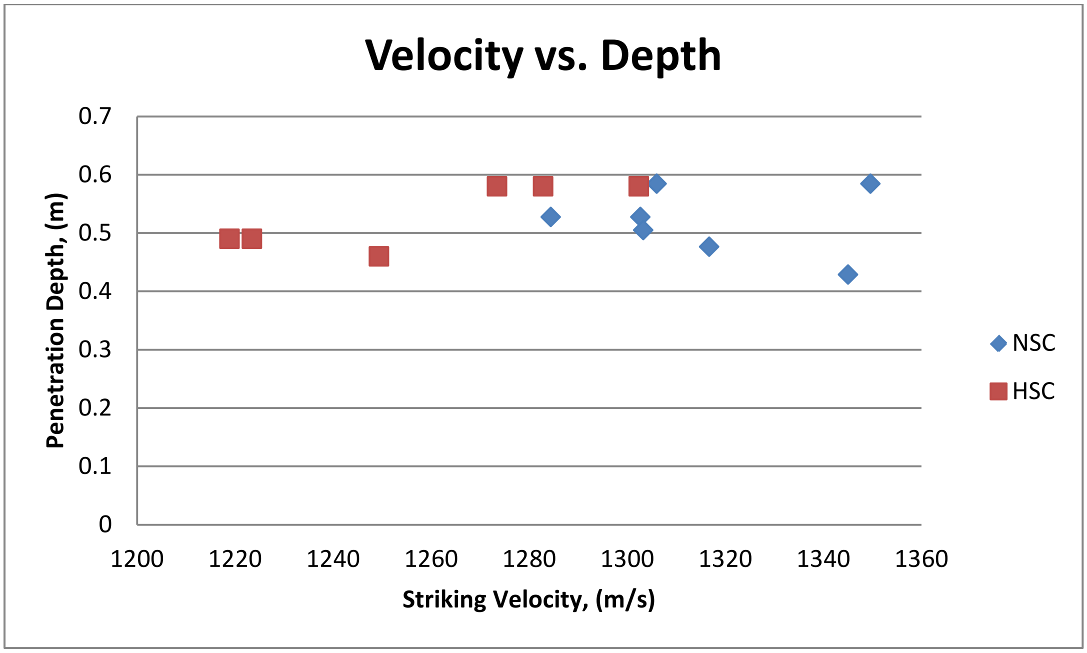

Figure 5.4: Striking Velocity vs. Measured Penetration Depth

Another explanation for the scatter in depths for similar velocities in the NSC data may be that the small data set. Due to the heterogeneous nature of concrete and the flaws that are inevitably present in any material predicting the pattern of fractures in concrete is quite difficult. With a much larger data set, a general upward trend may be present, with a range of depths per V_0 value.

5.4.2. Correlations Between Off-Centered Impacts and Penetration Depths. Most of the projectiles did not strike the blocks in the center. Instead, the impact points, ranged from 0 cm to about 14 cm (5.5 in) away from the center. The majority of the projectiles hit the block at or less than 5.1 cm (2 in) off-center. Figure 5.3 shows that, due to the small width of the blocks, an impact does not have to be off-center very much to result in some attenuation of the original shockwave by the first rarefactions. So, theoretically, it stands to reason that the farther off-center an impact occurs, the shallower the penetration depth will be. Figure 5.5, below, shows the measured penetration depths plotted in relation to the impact location, relative to the center of the block.

A regression analysis on the penetration depth vs. the distance off center of the impact using Minitab ® gives R^2 values of 0.623 for the NSC data and 0.078 for the HSC data. The regression data indicates that the impact location had a greater impact on the NSC blocks, but if the the data point at 0.14 m (5.5 in.) off center is removed, the new R2 value becomes 0.195 and the two data sets are more evenly matched. However, it is worth noting that despite being various distances off center, the projectile impacts on two NSC blocks and four HSC blocks resulted in holes extending the entire length of the block. According to the figure below, the penetration depths remain in the 0.40- 0.58 m (15.75-23 in.) range until the projectile strikes the block more than 0.14 m (5.5 in.) off-center. So, it may be possible that the variation in the penetration depths is more strongly related to imperfections in the concrete rather than the impact location.

Even though an off-center impact can result in some attenuation of the original shockwave, the compressive and tensile forces exerted on the concrete by the shockwave and rarefactions are extremely large when compared to the compressive and tensile strength of the material. This large difference in material strength versus the stresses experienced by the concrete can explain why the small amount of attenuation of the shockwave did not result in a measurable difference in the penetration depths.

5.4.3. Effect of Target Diameter on Penetration Depth. A generally accepted idea about target diameter to projectile diameter ratios assumes that edge effects within a target with a small target diameter to projectile diameter ratio have a significant effect on the final penetration depth. However, one study conducted by Frew, Forrestal, and Cargile in 2006 compared the penetration with targets that had three sets of target diameter to projectile diameter ratios-12, 18, and 24. The concrete targets, cast in steel culverts, had equal compressive strengths. The data showed a negligible effect on penetration depths due to the target diameter, but the damage to the front face of the target increased as the target diameter decreased. (16) However, the authors caution that the results may be due to the design parameters of the experiment.

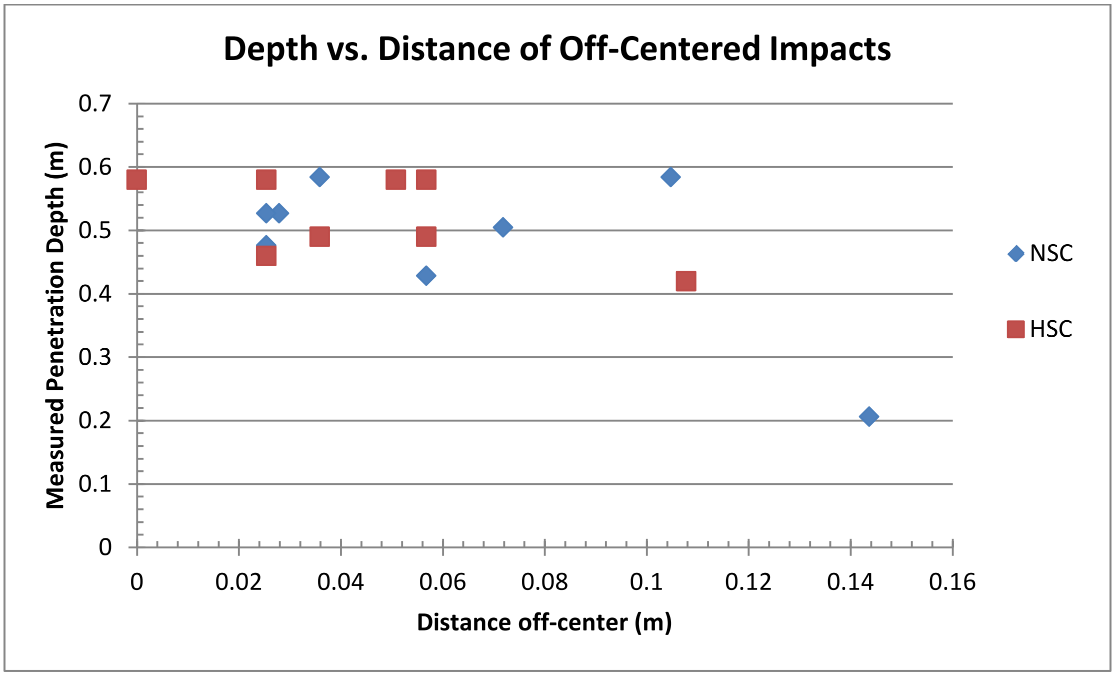

Figure 5.5: Off-center impacts vs. depths

Since the blocks used in this research were not cast in culverts, and the previously referenced study does not offer any suggestions as to how much the confinement around the targets affected penetration depth, it is difficult to say with certainty how much the measured penetration depths may have differed with wider blocks. The reflections of the shockwave and the pieces that fracture off the block as the shockwave travels through the material remove impact energy. The energy required to create fractures in the concrete block is the main mechanism by which the shockwave energy is dissipated. The energy that is used to fracture the front and sides of the block reduces the total energy used to penetrate deeper into the block. Therefore, the smaller blocks most likely result in more conservative penetration values.

5.5. VELOCITY MEASUREMENTS

As mentioned in Section 4.4, during the high strength concrete block tests, the projectile velocities were measured using both the high speed camera and the oscilloscope setup. During one test, neither the oscilloscope nor the camera triggered properly. For the other nine high strength tests, four (Blocks 12, 13, 14, and 18) yielded good agreement between the camera and oscilloscope velocities. The other five tests had measured differences from 99-481 m/s (325-1578 ft/s). There are several items which can account for the difference between the camera and oscilloscope velocities.

The 30 gage wire used for the screens in combination with being strung through notches on the top and bottom of the screen, resulted in difficulties keeping the wire taut in the screen. Also, the screens were strung at night, and used during the day. The increase in temperature allowed the wire to stretch which contributed to a looser wire in the velocity screens. Despite efforts to tighten the wire before the tests, on some screens the wire may have been looser than desired.

If the nose of the projectile did not strike a length of wire, and instead broke the wire with the middle or tail end, the measured velocity would be affected. A 7.5 cm (3 in.) difference in the expected position of the wire would result in a measured velocity with an error 270 m/s (889 ft/s) from the actual value. The wire could have been stretched and/or broken with a portion of the projectile other than the nose on the tests where the two measured velocity values differ significantly.

To prevent this issue, future velocity screens should consider securing the wire differently and placing the strands of wire closer together along the length of the screen. While there are other methods to construct velocity screens, this method using a continuous circuit of wire in a disposable frame was chosen since it was the most cost effective method. Due to the inconsistent oscilloscope velocities, along with the fact that the system needs to be perfected, the camera velocities were used for all analysis in this document.

6. CONCLUSIONS

Many factors affect projectile penetration of concrete, including projectile mass, material, diameter, nose shape, striking velocity, and concrete compressive strength. Estimating penetration depths becomes more complicated when considering the varied ways in which concrete fractures under a certain load, and that the imperfections within the matrix greatly influence where fractures begin and how they propagate. The photos of Blocks 1-20 show the varied different fracture patterns that occurred, despite being struck with very similar projectiles with velocities between 1220-1350 m/s (3674-4429 ft/s). The many paths that the fractures can propagate through result in a variety of fractured faces, which can result in a variety of crater depths for the same volume of concrete removed. The variability in where failure begins and how it spreads makes it unwise to assume that with a certain projectile mass, diameter, material, nose shape, and striking velocity one penetration depth will occur.

The Hugoniot analysis of the original shockwave and the rarefactions originating from the front corners of the block gives two theoretical assumptions. The first assumption, based on particle velocity and pressure calculations show that the stresses within the concrete greatly exceed the material strengths. At the impact point, both sets of blocks experienced compressive pressures upwards of 10 GPa and tensile pressures of more than 1.3 GPa, which dwarf the measured compressive strengths of 36.1 MPa and 46.0 MPa and the estimated tensile strengths of 3.6 and 4.6 MPa. With the large differences between concrete strengths and estimated stresses, the concrete will fracture until all of the impact energy has been dissipated. In the 20 experiments, the energy dissipated through fracturing material away from the block, breaking the back of the block into multiple pieces, and by moving the block pieces away from the block original location.

In addition to considering the magnitudes of the compressive and tensile stresses within the block, the location of impact relative to the center of the block must also be considered. As shown in Figure 5.3, an impact more than 5.1 cm off-center will result in the rarefaction catching up to the original shockwave and begin to attenuate the original shockwave. The farther off-center the impact occurs, the more time the rarefaction has to attenuate the original shockwave, which lowers the compressive pressures within the block. This theoretical analysis agrees with the trend-lines shown in Figure 5.5, which show that as the impact distance from the center increases, the measured penetration depth decreases.

The relationship between striking velocity and penetration depths did not have as strong a correlation as expected. The HSC data has an R^2 value of 0.725, indicating a moderately strong correlation, although data points lie both above and below the trend-line. The NSC data has an R^2 value of 0.027, which suggests a very weak relationship between striking velocity and penetration depth. Since the NSC blocks had varied penetration depths, but a consistent remaining volume of concrete, the weak correlation between penetration depth and velocity may have been affected by the varied fracture patterns that occurred within the block. However, the small sample size may not be able to show the whole picture; a variety of depths may occur for a given striking velocity and a large enough data set may show a stronger relationship between the two variables.
The small block width may have affected the penetration depths by allowing material (and energy) to be removed from the sides of the block as well as the front and back faces. The research cited in Reference (18) showed a negligible effect on penetration depth with changing target diameters. However, the concrete targets in the research had a steel culvert casing preventing concrete fracturing away from the sides of the block. In order to determine if the width of the blocks, target diameter: projectile diameter =18, affected the penetration values, more data would be needed for comparison, keeping the concrete strength, shape, and projectile characteristics the same while varying the target diameter: projectile diameter ratio.

With regard to which formulas most accurately predicted the experimental penetration depths, the values for Blocks 1-9 and Blocks 10-20 are tabulated in Table 10 and Table 11, respectively. The seven formulas used for comparison of the data with the outliers removed both under- and over-predicted the values. The UFC formula, amended to account for the copper projectile, most accurately estimated the NSC penetration, with an under-prediction of 8.7 %. The Kar formula most accurately estimated the HSC penetration, with an under-prediction of 16.6%. Several of the existing penetration formulas recommend a 15% safety factor, when using concrete penetration formulas. For the NSC data, using a 15% safety factor with the UFC formula should be sufficient, but using the Kar formula to predict projectile penetration of the HSC blocks requires a larger safety factor.

In conclusion, for the data sets presented here, for a given set of impact and target characteristics, there appears to be a range of possible penetration depths. For the high strength concrete, every impact above a certain velocity resulted in a hole that extended the length of the target, while the normal strength concrete had a variety of penetration depths despite the very similar striking velocities. The projectile striking location with respect to the center of the block does not seem to have a noticeable effect on the penetration depth until the impact occurred more than 0.14 m (5.5 in.) off center. For estimating penetration depths of EFPs, the UFC Formula provided the closest predictions for the NSC blocks, while the Kar Formula proved to be most accurate for the HSC blocks. Both formulas under-predicted the penetration depth, and due to the variable nature of concrete fracture, a safety factor should be included when using these formulas for design purposes.

BIBLIOGRAPHY

1. **W.P. Walters, J.A. Zukas.** *Fundamentals of Shaped Charges.* Baltimore : CMCPress, 1998. 0-471-62171-2.

2. **Jonas A. Zukas, William P. Walters.** *Explosive Effects and Applications.* s.l. : Springer, 2002.

3. **Jonas Zukas, Theodore Nicholas, Hallock Swift, Longin Greszczuk, Donald Curran.** *Impact Dynamics.* Malabar : Krieger Publishing Company, 1992. 0-89464-661-3

4. *A Review of Procedures for the Analysis and Design of Concrete Structures to Resist Missile Impact Effects.* **Kennedy, R.P.** s.l. : Nuclear Engineering Design, 1976, Vol. 37. 183-203.

5. *Effects of Impact and Explosion.* **National Defense Research Committee.** Washington, D.C. : s.n., 1946.

6. *Local impact effects of hard missiles on concrete targets.* **Q.M. Li, S.R. Reid, H.M. Wen, A.R. Telford.** s.l. : International Journal of Impact Engineering, 2005, Vol. 32. 224-284.

7. *An empirical equation for penetration depth of ogive-nose projectiles into concrete targets.* **Forrestal, M.J.** 4, s.l. : International Journal of Impact Engineering, 1994, Vol. 15. 395-405.

8. **Young, C.W.** *Penetration Equations.* Albuquerque : Sandia National Laboratories, 1997. SAND97-2426.

9. **Unified Facilities Criteria.** *Design of Structures to Resist Accidental Explosions.* 2008. UFC 3-340-02.

10. **David Lambert, 1Lt. Matthew Pope, Stanley Jones, Jonathan Muse.** *Soft-Recovery of Explosively Formed Penetrators.* Eglin AFB : Air Force Research Laboratory, Munitions Directorate, 2005. AFRL-MN-EG-TP-2005-7414.

11. *IED effects research at TNO Defence Security and Safety.* **Martijn van der Voort, Marnix Rhijnsburger.** Bruehl : 13th International Symposium on the Interaction of the Effects of Munitions with Structures, 2009.

12. **Mulligan, Phillip Russell.** *The Effects Select Physical Parameters Have on an Explosively Formed Projectile's Performance.* Rolla : Missouri University of Science & Technology, 2011.

13. **Cooper, Paul W.** *Explosives Engineering.* Hoboken : Wiley-VCH, Inc. , 1996. 0-471-18636-8.

14. **C.A. Hall, L.C. Chhabildas, W.D. Reinhart.** *Shock Hugoniot and Release States in Concrete Mixtures with Different Aggregate Sizes from 3 to 23 GPa.* Albuquerque : Sandia National Laboratories, 1997. SAND-97-2011C.

15. **Sidney Mindess, J. Francis Young, David Darwin.** *Concrete.* Upper Saddle River : Prentice Hall, 2003. p. 317. 0-13-064632.

16. **DiGiulian, Tony.** Calculating CRH. *NavWeaps.* [Online] 12 23, 2004. http://www.navweaps.com/index_tech/tech-094.htm.

17. **Donald E. Carlucci, Sidney S. Jacobson.** *Ballistics: Theory and Design of Guns and Ammunition.* Boca Raton : CRC Press, 2008. 9781420066180.

18. *The effect of concrete target diameter on projectile deceleration and penetration depth.* **D.J Frew, M.J Forrestal, J.D. Cargile.** s.l. : International Journal of Impact Engineering, 2006, Vol. 32, pp. 1584-1594.

VITA

Laurin Ashley Bookout was born in Anchorage, AK on January 8, 1987. In 2005 she graduated second in her class from John F. Hodge High School in St. James, MO. She then enrolled at the University of Missouri-Rolla, earning her B.S. in Civil Engineering in December 2009. After completing her Bachelor’s degree, Laurin decided to continue her studies and pursue a Master’s degree. Laurin completed the requirements received her M.S. in Explosives Engineering in December 2011.